Publication Year	2022
Acceptance in OA	2023-07-24T14:32:31Z
Title	HST Observations of the Globular Cluster NGC 6402 (M14) and Its Peculiar Multiple Populations
Authors	D'ANTONA, Francesca, Milone, Antonino P., Johnson, Christian I., TAILO, Marco, Vesperini, Enrico, Caloi, Vittoria, VENTURA, Paolo, MARINO, Anna, Flavia Dell'Agli
Publisher's version (DOI)	10.3847/1538-4357/ac3a70
Handle	http://hdl.handle.net/20.500.12386/34330
Journal	THE ASTROPHYSICAL JOURNAL
Volume	925

The Astrophysical Journal, 925:192 (17pp), 2022 February 1 https://doi.org/10.3847/1538-4357/ac3a70

HST Observations of the Globular Cluster NGC 6402 (M14) and Its Peculiar Multiple Populations

Francesca D'Antona[1], Antonino P. Milone[2], Christian I. Johnson[3], Marco Tailo[2,4], Enrico Vesperini[5], Vittoria Caloi[6], Paolo Ventura[1], Anna Fabiola Marino[7], and Flavia Dell'Agli[1]

[1] INAF–Osservatorio Astronomico di Roma, Via Frascati 33, I-00078 Monteporzio Catone (Roma), Italy; francesca.dantona@inaf.it, franca.dantona@gmail.com
[2] Dipartimento di Fisica e Astronomia "Galileo Galilei", Università di Padova, Vicolo dell'Osservatorio 3, IT-35122, Padova, Italy
[3] Space Telescope Science Institute, 3700 San Martin Dr., Baltimore, MD 21218, USA
[4] Dipartimento di Fisica e Astronomia "Augusto Righi", Università degli Studi di Bologna, Via Gobetti 93/2, I-40129 Bologna, Italy
[5] Department of Astronomy, Indiana University, Bloomington, IN 47401, USA
[6] INAF–IAPS Roma, Via Fosso del Cavaliere, Roma, IT-00133, Italy
[7] INAF–Osservatorio Astrofisico di Arcetri, Largo E. Fermi 5, I-50125, Firenze, Italy

Received 2021 September 7; revised 2021 November 15; accepted 2021 November 15; published 2022 February 4

Abstract

We present Hubble Space Telescope (HST) photometric results for NGC 6402, a highly reddened, very luminous Galactic globular cluster (GC). Recent spectroscopic observations of its red giant stars have shown a quite peculiar behavior in the chemistry of its multiple populations. These results have prompted UV and optical HST observations aimed at obtaining the cluster's "chromosome map" (ChM), an efficient tool for classifying GCs and characterizing their multiple populations. We find that the discontinuity in the abundance distributions of O, Mg, Al, and Na inferred from spectroscopy is more nuanced in the ChM, which is mostly sensitive to nitrogen. Nevertheless, photometry in optical bands reveals a double main sequence, indicating a discontinuity in the helium content of the populations. The population with the largest chemical anomalies (extreme) peaks at a helium mass fraction $Y \sim 0.31$. This helium content is consistent with results from the analysis of the distribution of horizontal branch stars and the spectrophotometry of the red giants. The ChM and the color–magnitude diagrams are compared with those of NGC 2808, a prototype GC with helium abundances up to $Y \gtrsim 0.35$, and both confirm that NGC 6402 does not host stellar populations with such extreme helium content. Further, the ChM reveals the presence of a group of stars with higher metallicity, thus indicating that NGC 6402 is a Type II cluster. The modalities of formation of the multiple populations in NGC 6402 are briefly surveyed, with main attention on the asymptotic giant branch and supermassive star models, and on possible cluster merging.

Unified Astronomy Thesaurus concepts: Globular star clusters (656); HST photometry (756); Hubble Space Telescope (761); Stellar evolution (1599); Stellar evolutionary models (2046); Nucleosynthesis (1131)

1. Introduction

In spite of being the 10th best cluster in terms of luminosity (and mass) among Galactic globular clusters (GCs), NGC 6402 (M14) has not been subject to close scrutiny like other massive GCs, being located close to the Galactic plane and highly reddened ($E(B-V) \simeq 0.6$). The cluster has a moderately high metallicity of $[\mathrm{Fe/H}] = -1.13 \pm 0.05$ (Johnson et al. 2019), which is similar to that of NGC 2808, the cluster prototype for the study of multiple populations. Hubble Space Telescope (HST) photometry from the Piotto et al. (2002) snapshot survey showed that NGC 6402 is an example of a "second-parameter" cluster (for a recent discussion, see Tailo et al. 2020), as its horizontal branch (HB) morphology is too blue for its metallicity. In fact, the HB includes only a few stars on the red side of the RR Lyrae gap and extends to high T_{eff}. The most complete ground-based photometry (B and V) down to the upper main sequence (MS) is provided by Contreras Peña et al. (2013). An analysis and a catalog of 110 RR Lyrae stars are given by Contreras Peña et al. (2018), who also summarize the possible indications that this cluster has an extragalactic origin.

The light-element abundances in Galactic (but also in extragalactic) GCs display large variations, with typical anticorrelations indicating the presence of two or more chemically distinct groups of stars (see, e.g., Gratton et al. (2019) for a recent comprehensive summary). While the elemental abundances in some stars are similar to those of halo stars having the same metallicity (population 1G), the majority of stars show abundance patterns typical of gas processed at very high temperature ($T \sim 30$–100 MK, depending on the locus of processing) by proton capture reactions (population 2G[8]). The abundance of helium in the standard halo and in the 1G of GCs is settled on the big bang composition ($Y \sim 0.25$ in mass fraction). However, it is larger in the p-processed gas of enriched populations and reaches values up to $Y \sim 0.35$ in the "extreme" groups present in a few massive clusters, such as ω Cen and NGC 2808. In these clusters, the 2G itself is split into separate groups, highlighted photometrically by splits of the MS due to the different value of Y in each of them (Bedin et al. 2004; D'Antona et al. 2005; Lee et al. 2005; Piotto et al. 2007; Tailo et al. 2016; Bellini et al. 2017), and, in NGC 2808, by the

---

[8] The nomenclature here follows that of Milone et al. papers. The name "1G" actually means "first generation" to be considered as the generation of stars from which any population with signatures of hot-proton capture nucleosynthesis necessarily follows (second generation or 2G), either within $\sim 10^6$ yr (supermassive star model) or within $\sim 10^8$ yr (AGB model). Where confusion with previous definitions arises we will clarify them.

grouping of different abundance anomalies revealed by high-dispersion spectroscopy (Carretta 2015). A standard value of $Y \sim 0.35$ is quoted in the literature for the blue MS of NGC 2808 (e.g., D'Antona et al. 2005), and $Y = 0.37$ is derived for the more complex case of ω Cen (e.g., Tailo et al. 2016).

In recent years, photometry in the UV bands, especially in the HST bands of the UV WFC3/UVIS filters F275W and F336W, complemented with the blue filter F438W, has proven to be a powerful way of acquiring information on multiple populations, thanks to the sensitivity of these filters to C, N, and O abundance variations. The results of the HST UV legacy survey (Piotto et al. 2015) permitted classifying GCs in terms of their "chromosome map" (ChM; Milone et al. 2017), a pseudo-two-color diagram where stars belonging to different populations cluster in different loci, as shown by a comparison with the results of high-dispersion spectroscopy (Marino et al. 2019). Thus spectra and HST UV photometry are useful complementary tools for investigating multiple populations and attempting to reach a full understanding of their formation.

Both tools have shown that the most massive GCs exhibit the most complex chemical patterns. C–N and Na–O anticorrelations are commonly present in all GCs, but the most massive clusters also show Mg–Al, and sometimes even Mg–K anticorrelations (e.g., Cohen & Kirby 2012; Mucciarelli et al. 2015; Carretta 2021). A small fraction of Galactic GCs show significant iron abundance variations, with very significant cluster-to-cluster differences in the percentage of stars with higher metallicity and in the degree of iron enhancement (see, e.g., Johnson et al. 2015, and references therein). These "iron-complex" clusters, discovered by spectroscopy and by a split red giant branch (RGB) in *hk*-narrowband photometry (e.g., Lee 2015; Lim et al. 2015), have been also identified by their remarkably complex ChM, as higher-metallicity stars are located at the red side of the standard ChM loci, and they are dubbed "Type II" clusters (Milone et al. 2017). Most Type II clusters have HB morphologies that extend to very high temperatures, which commonly identify these stars as descendants of the high-helium population (e.g., D'Antona & Caloi 2004, 2008). Finally, the more massive clusters contain a larger fraction, up to more than 80%, of stars belonging to the anomalous 2G (see Figure 22 in Milone et al. 2017).

There is consensus that the gas forming the 2G has been exposed to high temperatures, but the site and modalities of the consequent nuclear processing are still being debated. No models are fully consistent with the formation of multiple populations (see, e.g., Gratton et al. 2019). Collecting data and analyzing cluster-to-cluster differences in the chemical patterns helps to discriminate among models and collect information on the formation process of these fundamental galaxy constituents.

NGC 6402 also hosts multiple populations, as shown by Johnson et al. (2019), who determined the chemical composition of 41 NGC 6402 giants by means of high-resolution spectra obtained with the Magellan-M2FS instrument. The Johnson et al. (2019) analysis highlighted interesting peculiarities in the abundance patterns of light elements, which have prompted the present investigation. The giants in the sample were shown to belong either to the P1 (1G), 12/35 giants ∼34%, or to a very mildly polluted population (P2, which here we will call 2G mild[9]; 14/35 giants ∼40%), or to a population with "extreme" anomalies (E, 9/35 giants ∼26%). The cluster is apparently lacking giants with "intermediate" (I) compositions between the 2G mild and 2G extreme or E groups, and this may be due to the precise modalities of formation. The gap in chemistry is a further indication that the formation of multiple populations occurs discontinuously, in bursts. It may also suggest that different polluters are at play in forming the gas of the E and 2G mild populations. In fact Johnson et al. (2019) proposed that the E group is born in the gas processed in supermassive stars (hereinafter SMSs; Denissenkov & Hartwick 2014), formed in the early phases of cluster formation by the merging of massive stars, and that the P2 (2G mild) group is formed much later on, by AGB winds very diluted with reaccreting pristine gas, following the model first proposed by D'Ercole et al. (2008); see also Calura et al. (2019) for recent simulations.

We refer the reader to Gratton et al. (2019) for a detailed summary of models proposed in the literature, and limit a more detailed analysis to the formation of the second population in matter polluted by SMSs (Denissenkov & Hartwick 2014; Denissenkov et al. 2015; Gieles et al. 2018) and to the AGB model (see, e.g., D'Ercole et al. 2008; Bekki 2011; D'Antona et al. 2016; Bekki & Tsujimoto 2017; Ventura et al. 2018). These two models have qualitatively survived a preliminary scrutiny, although with well-recognized difficulty. The main problems still hampering their validation are, (i) for the AGB model, the issue of the oxygen and sodium abundances in extreme stars and, (ii) for the SMS model, the formation itself of such objects, and the necessity of freezing their H-burning stage to incomplete core hydrogen burning. Consequently, observations that may help us to understand whether two polluting sources are needed in the complex formation of GCs, or at least of some of them, are an issue that deserves attention and a deep analysis.

Recently attention has been also focused on the possible paths of formation of iron-complex clusters, either along the same paths of formation of the multiple populations (D'Antona et al. 2016; Lacchin et al. 2021; Wirth et al. 2021), or by considering the possible merging between clusters differing in metallicity (van den Bergh 1996; Amaro-Seoane et al. 2013; Bekki & Tsujimoto 2016; Gavagnin et al. 2016; Khoperskov et al. 2018). As NGC 6402 will be confirmed as a Type II cluster, we will also ask whether this feature offers clues for the formation model.

The HST UV observations of the central regions of NGC 6402 were planned to further constrain the models, by adding photometric information useful to identifying different stellar populations and combining this information with the spectroscopic analysis. In this work we present the results of the UV photometry of the core region of the cluster, its color–magnitude diagrams (CMDs), and the ChM, and compare them with those of the most similar cluster in terms of mass and metallicity, NGC 2808. We also present and compare with NGC 2808 the observations of a deep CMD in the bands F475W and F814W obtained in parallel-field exposures, and give a preliminary analysis of the HB stellar distribution.

We show that NGC 6402 hosts less extreme populations than NGC 2808, as could also be evinced from the lack of extreme Mg depletion in oxygen-poor giants. The maximum helium abundance in the E population is $Y \sim 0.31$, much smaller than the abundance required by present-day massive AGB models and by the SMS models so far analyzed to be consistent with

---

[9] The Johnson et al. (2019) work follows the nomenclature by Carretta et al. (2018), who subdivided the stars in NGC 2808 into five groups with increasing anomalies: P1, P2, I1, I2, and E. Roughly these groups correspond to the ChM groups B (P1), C (P2), D (I1 and I2), and E (E) by Milone et al. (2015)—see Section 5. Here we will use the term 1G (P1), 2G mild (P2), and 2G extreme or E. Further nomenclature will be added in Section 3.

Table 1
Description of the HST Images Used in the Paper

Camera	Filter	$N \times$ Exp. Time
	Primary Field	
UVIS/WFC3	F275W	987 s + 988 s + 10 × 1050 s + 3 × 1172 s + 1181 s
UVIS/WFC3	F336W	11 × 761 s
UVIS/WFC3	F438W	2 × 100 s + 10 × 348 s
UVIS/WFC3	F814W	10 × 110 s
	Parallel Field	
WFC/ACS	F475W	350 s + 822 s + 2 × 890 s + 10 × 990 s + 1046 s + 1091 s
WFC/ACS	F814W	35 s +350 s + 10 × 619 s + 719 s

Note. All images were collected on 2021 February 6–13 as part of GO-16283 (PI: F. D'Antona).

strong oxygen reduction in the abundances. We briefly discuss the consequences of these results.

2. Observations and Data Reduction

To investigate multiple stellar populations we exploited HST images of two fields of view in the direction of NGC 6402 as part of GO-16283 (PI: F. D'Antona). The primary field includes the cluster center and has been observed through the F275W, F336W, F438W, and F814W filters of the Ultraviolet and Visual Channel of the Wide Field Camera 3 (UVIS/WFC3). Parallel observations have been conducted with the Wide Field Channel of the Advanced Camera for Surveys (WFC/ACS) through the F475W and F814W bands. Additional information on the data set is provided in Table 1.

Photometry and astrometry were carried out with the computer program KS2 by using images corrected for effects of poor charge transfer efficiency of the UVIS/WFC3 and WFC/ACS detectors (Anderson & Bedin 2010). The KS2 program was written by Jay Anderson, and is the evolution of kitchen_sink, originally developed to reduce two-filter ACS/WFC images (Anderson et al. 2008). KS2 follows different recipes to derive stellar fluxes and positions. The first method measures the stars in each exposure independently, by fitting the appropriate effective point-spread function (PSF) models. The various measurements are then averaged together to get the best estimates of magnitudes and positions. This method provides the best measurements of bright stars. To measure faint stars that have not enough flux to be properly constrained by the PSF fit, KS2 combines the information from all exposures by fixing the average stellar positions from all exposures. After subtracting neighbor stars, it measures the faint stars by means of aperture photometry. We refer to papers by Sabbi et al. (2016) and Nardiello et al. (2018) for details on KS2.

Stellar positions have been corrected for geometric distortion by using the solutions presented in Bellini & Bedin (2009) and Bellini et al. (2011). Photometry has been calibrated to the Vega magnitude system by using the zero-points of the WFC/ACS and UVIS/WFC3 filters available at the Space Telescope Science Institute web pages. Since we are interested in investigating multiple populations, we selected the sample of well-measured stars, which are relatively isolated and well fitted by the PSF (see Milone et al. 2009 for details). To do this, we exploited the diagnostics provided by the KS2 program, including the magnitude rms, the fraction of flux in the aperture due to neighbors, and the quality of the PSF fit. Finally, the photometry was corrected for differential reddening by using the method and computer program described in Milone et al. (2012a).

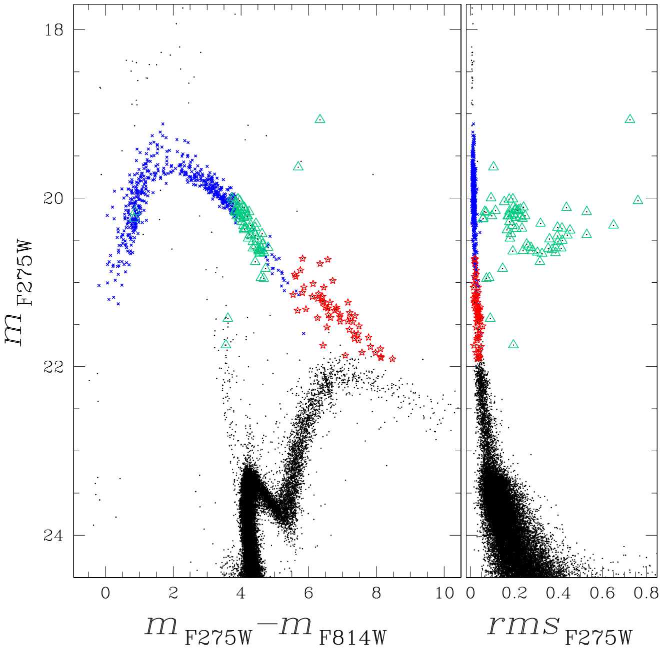

Figure 1. Left panel: $m_{\rm F275W}$ vs. $m_{\rm F275W} - m_{\rm F814W}$ CMD of NGC 6402 for stars in the central field. Right panel: $m_{\rm F275W}$ against the rms of the $m_{\rm F275W}$ measurements. HB non-variable stars, AGB stars, and variable stars are colored blue, red, and aqua, respectively.

3. Photometric Diagrams of NGC 6402

Differential reddening–corrected photometry has been used to build photometric diagrams that are sensitive to multiple stellar populations.

3.1. The CMDs

The left panel of Figure 1 shows $m_{\rm F275W}$ versus $m_{\rm F275W} - m_{\rm F814W}$ for stars in the central field. Thanks to the wide color baseline, this CMD maximizes the effective-temperature differences among MS and RGB stars with similar luminosities and provides an exquisite tool for identifying stellar populations with different helium abundances. The right panel of Figure 1 shows the rms of the F275W magnitude determinations against $m_{\rm F275W}$. The fact that some stars exhibit large rms values, as compared with the bulk of stars of similar magnitude, is a signature of stellar variability. The sample of candidate variables comprises 71 stars, which are represented with aqua triangles in both panels of Figure 1, including 65 candidate RR Lyrae stars, 2 blue stragglers, 2 hot HB stars, and 2 post-HB stars.

Two additional CMDs are provided in Figure 2 for stars in the central field. A split RGB is clearly visible in the $m_{\rm F336W}$ versus $m_{\rm F336W} - m_{\rm F438W}$ CMD, which is the HST analog of U versus $U - B$ and is mostly sensitive to nitrogen variations (Marino et al. 2008). The $m_{\rm F814W}$ versus $C_{\rm F275W,F336W,F438W}$ CMD also reveals a broad RGB, thus confirming that NGC 6402 hosts stellar populations with different light-element abundances. Intriguingly, the AGB of NGC 6402 exhibits a wide $C_{\rm F275W,F336W,F438W}$ intrinsic spread, which is comparable with that of RGB stars with similar luminosity. This fact

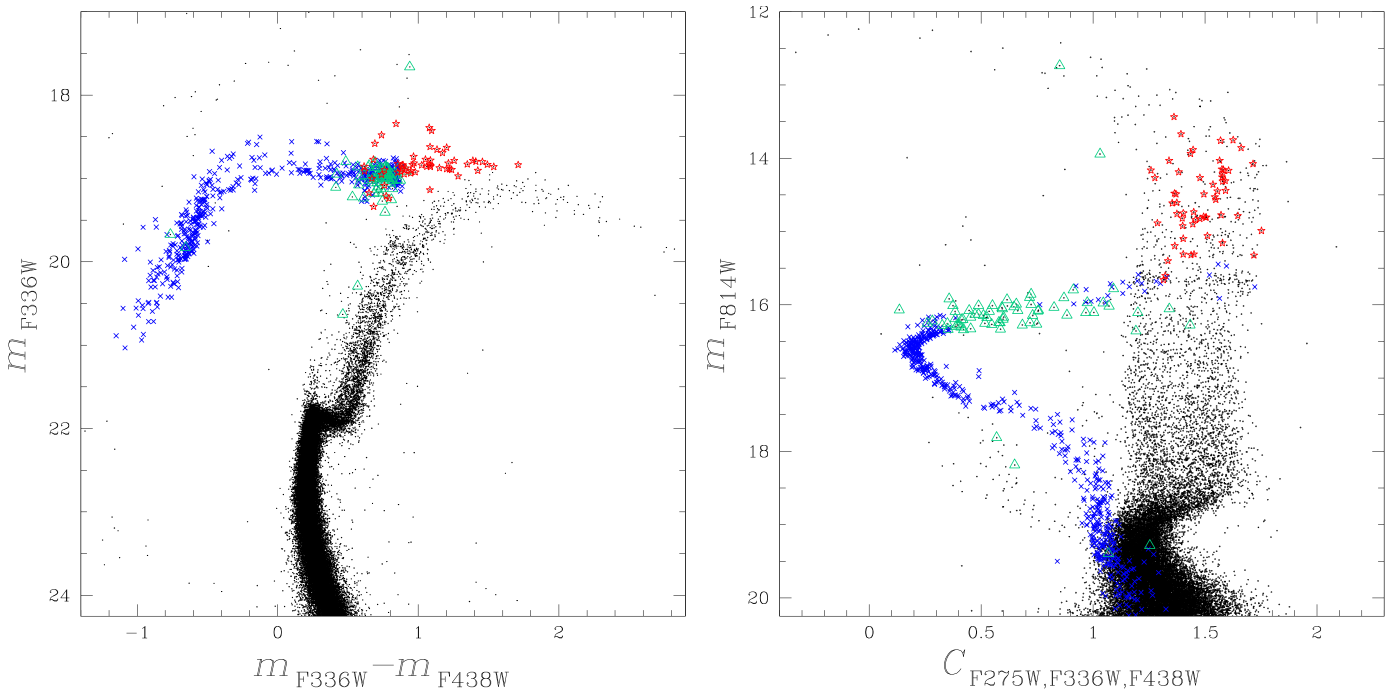

Figure 2. $m_{\rm F336W}$ vs. $m_{\rm F336W} - m_{\rm F438W}$ CMD (left) and $m_{\rm F814W}$ vs. $C_{\rm F275W,F336W,F438W}$ pseudo-CMD for stars in the central field. The colors are the same as those in Figure 1.

demonstrates that, similar to the RGB, the AGB of NGC 6402 hosts multiple populations.

3.2. The ChM

The ChM is a pseudo-two-color diagram of MS, RGB, or AGB stars obtained from appropriate filter combinations that maximize the separation among stellar populations in GCs (Milone et al. 2015; Marino et al. 2017). However, the ChM differs from a simple two-color diagram because the sequence of stars is verticalized on both colors.

Here, we derived two distinct ChMs of RGB stars based on the $m_{\rm F814W}$ versus $m_{\rm F275W} - m_{\rm F814W}$ CMD, the $m_{\rm F814W}$ versus $m_{\rm F336W} - m_{\rm F438W}$ CMD, and the $m_{\rm F814W}$ versus $C_{\rm F275W,F336W,F438W}$ pseudo-CMD by following the recipe by Milone et al. (2015, 2017; see their Section 3.1).[10] The $\Delta_{C\,\rm F275W,F336W,F438W}$ versus $\Delta_{\rm F275W-F814W}$ ChM of RGB stars and the corresponding Hess diagram are shown in the upper panels of Figure 3, whereas in the bottom panels we plot $\Delta_{\rm F336W-F438W}$ against $\Delta_{\rm F275W-F814W}$. The ChM is shown again in the left panel of Figure 4. It highlights the group of 1G stars, located around the origin of the map and colored green, and an extended 2G, where we identified four subpopulations of $2\rm G_A$, $2\rm G_B$, $2\rm G_C$, and $2\rm G_D$ stars. Stars that are likely members of these groups are colored orange, cyan, blue, and red, respectively. NGC 6402 is affected by a large average reddening ($E(B-V) = 0.6$; Harris 1996) and by significant reddening variations across the field of view. To verify that the multiple populations identified on the ChM and the CMD are not artifacts due to differential reddening, we checked that each

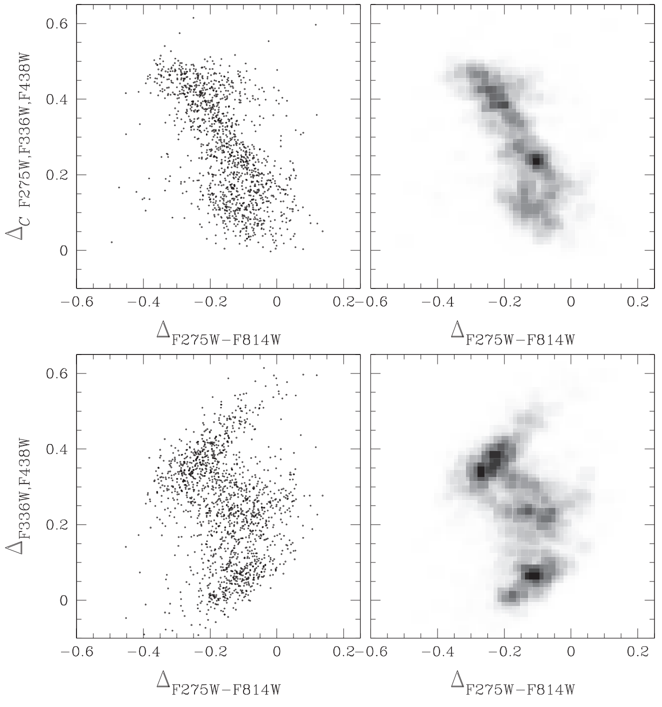

Figure 3. Left panels show $\Delta_{C\,\rm F275W,F336W,F438W}$ vs. $\Delta_{\rm F275W-F814W}$ (top) and $\Delta_{\rm F336W-F438W}$ vs. $\Delta_{\rm F275W-F814W}$ ChMs (bottom) of RGB stars in NGC 6402. The corresponding Hess diagrams are plotted in the right panels.

---

[10] In a nutshell, to derive the $\Delta_{\rm F275W,F814W}$ pseudocolor of RGB stars, we divided the $m_{\rm F814W}$ versus $m_{\rm F275W} - m_{\rm F814W}$ CMD into 0.1 mag wide magnitude bins and calculated the 4th and 96th percentiles of the $m_{\rm F275W} - m_{\rm F814W}$ color distributions of RGB stars in each bin. These quantities have been associated with the median values of the F814W magnitude distribution of the stars in each bin and have been linearly interpolated to derive the blue and red boundaries of the RGB. The $\Delta_{\rm F275W,F814W}$ pseudocolor has been derived by means of Equation (1) from Milone et al. (2017), which transforms the CMD into a verticalized diagram, where the blue and red RGB boundaries translate into vertical lines with $\Delta_{\rm F275W,F814W} = 0$ and $\Delta_{\rm F275W,F814W} = -W_{\rm F275W,F814W}$, where $W_{\rm F275W,F814W} = 0.34$ mag is the RGB width calculated 2.0 F814W magnitudes above the MS turnoff. A similar approach has been adopted to derive the $\Delta_{C\,\rm F275W,F336W,F438W}$ pseudocolor but by using the $m_{\rm F814W}$ versus $C_{\rm F275W,F336W,F438W}$ pseudo-CMD. In this case, the diagram has been verticalized by assuming Equation (2) from Milone et al. (2017) and the $C_{\rm F275W,F336W,F438W}$ RGB width of $W_{\rm F275W,F336W,F438W} = 0.48$ mag. See Milone et al. (2017) for details.

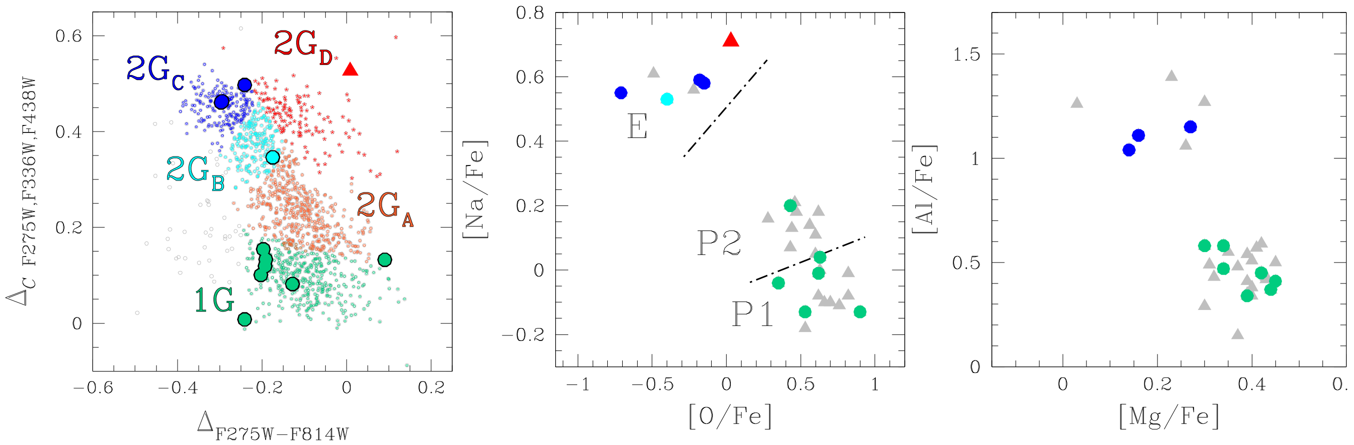

Figure 4. Reproduction of the $\Delta_{CF275W,F336W,F438W}$ vs. $\Delta_{F275W-F814W}$ ChM of Figure 3 (left panel). The middle and left panels show the sodium–oxygen and magnesium–aluminum anticorrelations, respectively, from Johnson et al. (2019). The dashed–dotted lines in the middle panel separate the populations of P1, P2, and E stars defined by Johnson and collaborators. The 1G, $2G_A$, $2G_B$, $2G_C$, and $2G_D$ stars, selected from the ChM, are colored aqua, orange, cyan, blue, and red, respectively. Stars for which both photometry and spectroscopy are available are represented with large colored symbols.

population is distributed in the entire field of view. Moreover, we divided the internal field into 39 quadrants and analyzed the ChM of stars in each of them. All the five stellar populations identified in Figure 4 are present in the ChM of stars in each quadrant, proving that they are real features of NGC 6402.

The $2G_D$ stars define a tail of stars in the ChM with redder $\Delta_{F275W-F814W}$ values than the bulk of stars with similar $\Delta_{CF275W,F336W,F438W}$ pseudocolors. This region of the ChM is typically populated by stars with enhanced iron and/or C+N+O abundance, and is a distinctive feature of Type II GCs (Milone et al. 2017).

By extending the procedure by Zennaro et al. (2019; see their Section 3.3) to the ChM plotted in Figure 4, we find that the 1G hosts $27.9\% \pm 2.3\%$ of the studied RGB stars. The selected groups of 2G stars include $34.6\% \pm 2.4\%$ ($2G_A$), $16.1\% \pm 2.0\%$ ($2G_B$), $12.9\% \pm 1.4\%$ ($2G_C$), and $8.4\% \pm 1.3\%$ ($2G_D$).

To infer the helium content of stellar populations, we adopted for NGC 6402 the method widely used by our group and used to constrain helium variations in about 60 GCs (e.g., Milone et al. 2018; Lagioia et al. 2019). In a nutshell, we derived the RGB fiducial lines of each population in the m_{F814W} versus $m_X - m_{F814W}$ CMD, where $X = F275W$, F336W, or F438W. We defined five equally spaced F814W magnitude values in the interval between $m_{F814W} = 14.8$ and 18.0. For each value we calculated the $m_X - m_{F814W}$ color difference between each fiducial line and the 1G ones. The comparison between the observed colors and an appropriate grid of synthetic spectra with different abundances of He, C, N, and O provides an estimate of the relative abundances of these elements.

The results are listed in Table 2 and they show that group $2G_C$ is highly helium-enhanced, by $\Delta Y \sim 0.05$ with respect to the 1G and the $2G_A$, which are both assumed to have pristine helium abundance ($Y \sim 0.25$).

Both $2G_B$ and $2G_C$ are enriched in nitrogen with respect to the 1G by more than 1 dex and depleted in carbon and oxygen by ~0.4 and 0.8 dex, respectively. On the other hand, population $2G_A$ has similar C and O abundances to the 1G but is enriched in [N/Fe] by ~0.6 dex. We did not infer the chemical composition of $2G_D$ stars, due to the enhanced metallicity of these stars. Since variations in iron significantly affect the stellar colors (and it would be challenging to disentangle the effect of helium and iron), we are not able to provide robust determinations of both helium and metallicity for these stars. Nevertheless, given the extreme $\Delta_{CF275W,F336W,F438W}$ pseudocolor, it would be reasonable to suggest that these $2G_D$ stars have extreme chemical composition, and hence high helium and nitrogen content, and are depleted in oxygen and carbon. If this hypothesis is correct, $2G_D$ stars are the RGB counterparts of a fraction of blue MS stars.

Table 2
Chemical Composition of Stellar Populations Relative to 1G Stars

Pop.	ΔY	Δ[C/Fe]	Δ[N/Fe]	Δ[O/Fe]
$2G_A$	0.000 ± 0.010	0.00 ± 0.20	0.60 ± 0.15	-0.10 ± 0.10
$2G_B$	0.037 ± 0.007	-0.40 ± 0.20	1.10 ± 0.10	-0.80 ± 0.15
$2G_C$	0.051 ± 0.009	-0.40 ± 0.20	1.20 ± 0.15	-0.80 ± 0.15

Note. We assumed all populations have $[Fe/H] = -1.10$ and adopted for the 1G $Y = 0.25$, solar C and N content, and $[O/Fe] = 0.3$.

3.2.1. Comparison with Johnson et al. (2019)

As discussed in the introduction, the first evidence of multiple populations in NGC 6402 was provided by Johnson et al. (2019), who analyzed 41 giant stars by using high-resolution spectra collected with Magellan-M2FS. They inferred the chemical abundances of 11 elements and identified three main stellar populations based on their position in the [Na/Fe] versus [O/Fe] plane. The middle panel of Figure 4 reproduces the sodium–oxygen anticorrelation by Johnson and collaborators and highlights the three populations of P1, P2, and E stars identified by these authors.

To further constrain the chemical composition of stellar populations identified along the ChM, we exploited 11 stars for which both photometry and spectroscopy from Johnson et al. (2019) are available (large colored symbols in Figure 4).

The results are listed in Table 3, where we show for each population with available spectroscopic targets, the average elemental abundance, the random mean scatter, and the number of spectroscopic targets. We find that 1G stars have nearly solar sodium content and are enhanced in both oxygen and magnesium.

Table 3
Chemical Composition of 1G, $2G_B$, $2G_C$, and $2G_D$ Stars of NGC 6402 Inferred from the Chemical Abundances Derived by Johnson et al. (2019)

	Population	Mean	rms	N
[O/Fe]	1G	0.58	0.19	6
	$2G_B$	−0.40	⋯	1
	$2G_C$	−0.35	0.32	3
	$2G_D$	0.03	⋯	1
[Mg/Fe]	1G	0.38	0.06	7
	$2G_C$	0.19	0.07	3
[Al/Fe]	1G	0.45	0.06	7
	$2G_B$	1.27	⋯	1
	$2G_C$	1.10	0.06	3
	$2G_D$	0.90	⋯	1
[Si/Fe]	1G	0.30	0.08	7
	$2G_B$	0.35	⋯	1
	$2G_C$	0.38	0.02	3
	$2G_D$	0.66	⋯	1
[Na/Fe]	1G	−0.01	0.11	7
	$2G_B$	0.53	⋯	1
	$2G_C$	0.57	0.02	3
	$2G_D$	0.71	⋯	1
[Ca/Fe]	1G	0.29	0.05	7
	$2G_B$	0.42	⋯	1
	$2G_C$	0.38	0.01	3
	$2G_D$	0.33	⋯	1
$[Fe/H]_I$	1G	−1.14	0.04	7
	$2G_B$	−1.10	⋯	1
	$2G_C$	−1.14	0.04	3
	$2G_D$	−1.05	⋯	1
$[Fe/H]_{II}$	1G	−1.15	0.04	7
	$2G_B$	−1.11	⋯	1
	$2G_C$	−1.14	0.04	3
	$2G_D$	−1.06	⋯	1
[Cr/Fe]	1G	0.04	0.07	7
	$2G_B$	0.13	⋯	1
	$2G_C$	0.13	0.07	3
	$2G_D$	0.06	⋯	1
[La/Fe]	1G	0.28	0.02	7
	$2G_B$	0.33	⋯	1
	$2G_C$	0.32	0.14	3
	$2G_D$	0.18	⋯	1
[Eu/Fe]	1G	0.32	0.06	6
	$2G_B$	0.36	⋯	1
	$2G_C$	0.41	0.02	2
	$2G_D$	0.31	⋯	1

In contrast, $2G_C$ is depleted in both [O/Fe] and [Mg/Fe] and enhanced in [Na/Fe], with respect to the 1G.

The comparison between spectroscopic and photometric results provides the opportunity to associate the populations identified by this paper and by Johnson et al. (2019). Clearly the 1G corresponds to the population P1 by Johnson and collaborators, while their population E is composed of stars in the groups $2G_B$, $2G_C$, and $2G_D$.

It would be tempting to associate the $2G_A$ stars identified on the ChM with the P2 by Johnson et al. (2019), as they exhibit moderate enhancement in N and Na, respectively, with respect to the 1G. Unfortunately there are no elemental abundances for $2G_A$ stars. Moreover, the only P2 star with available photometry seems to be located on the 1G of the ChM despite the fact that it is sodium-enhanced by more than 0.2 dex with respect to the bulk of 1G stars. More data are needed to establish whether the $2G_A$ is composed of 1G stars or if the analyzed P2 stars have large photometric and/or spectroscopic uncertainties.

3.3. Parallel-field Photometry

The $m_{\rm F814W}$ versus $m_{\rm F475W} - m_{\rm F814W}$ CMD corrected for differential reddening of stars in the parallel field is plotted in Figure 5(a). Clearly, NGC 6402 exhibits a split MS in the magnitude interval $20.0 < m_{\rm F814W} < 22.5$ and the two sequences seem to merge together along the MS turnoff (MSTO) and the subgiant branch (SGB). To further demonstrate that the double MS is not due to reddening variations, we verified that red and blue MS stars are distributed along the entire field of view, and that the double MS is evident in the CMDs of stars of each of the nine quadrants that compose the field of view.

To estimate the fraction of stars in the blue and red MSs we adopted the procedure illustrated in Figure 5. In a nutshell, we selected the region of the CMD where the MS split is evident (panel (a)) and derived the fiducial lines of the red and blue MSs (red and blue lines, respectively, in panel (b)). These two lines were used to verticalize the MS, in such a way that the fiducial lines of the blue and the red MS translate into two vertical lines with color residuals $\Delta_{\rm F475W,F814W} = 0$ and $\Delta_{\rm F475W,F814W} = 1$, respectively (panel (c); see Milone et al. 2015 for details). Finally, the $\Delta_{\rm F475W,F814W}$ histogram distribution plotted in panel (d) was fitted with a function provided by the sum of two Gaussian curves, by means of least squares. From the area of the two Gaussian components (red and blue curves in panel (d) of Figure 5) we infer that $65.2\% \pm 2.3\%$ of the stars belong to the red MS, while the blue MS is composed of the remaining $34.8\% \pm 2.3\%$ of MS stars.

In monometallic GCs the $m_{\rm F475W} - m_{\rm F814W}$ color split of MS stars is due to helium variations. To infer the average helium difference between blue MS and red MS stars we compared the observed MSs with appropriate isochrones from the ATON database (Tailo et al. 2016, 2020) with different helium abundances by using the procedure illustrated in Figure 6.

We adopted for all isochrones the same iron abundance, $[{\rm Fe/H}] = -1.1$, and $[\alpha/{\rm Fe}] = 0.3$ as in Johnson et al. (2019). The isochrone with $Y = 0.25$ that provides the best fit with the observed MSTO, SGB, and red MS was derived as in Tailo et al. (2020) and corresponds to an age of 12.50 ± 0.75 Gyr, a distance modulus of $(m{-}M)_0 = 14.76$ mag, and reddening of $E(B{-}V) = 0.62$ mag.

To derive the helium abundance of the blue MS, we defined a grid of six reference magnitude values in the interval where the split MS is clearly visible. Specifically, the reference magnitudes range from $m_{\rm F814W} = 20.4$ to $m_{\rm F814W} = 21.4$ in steps of 0.20 mag. To infer the relative helium content of the two MSs, we first calculated the $m_{\rm F475W} - m_{\rm F814W}$ color difference between the fiducial lines of the red and blue MSs corresponding to the six magnitude values. Then, we considered a grid of helium-enhanced isochrones with Y ranging from 0.250 to 0.385 in steps of 0.005. We derived the color differences between the best-fit isochrone with $Y = 0.25$ and each helium-enhanced isochrone and compared

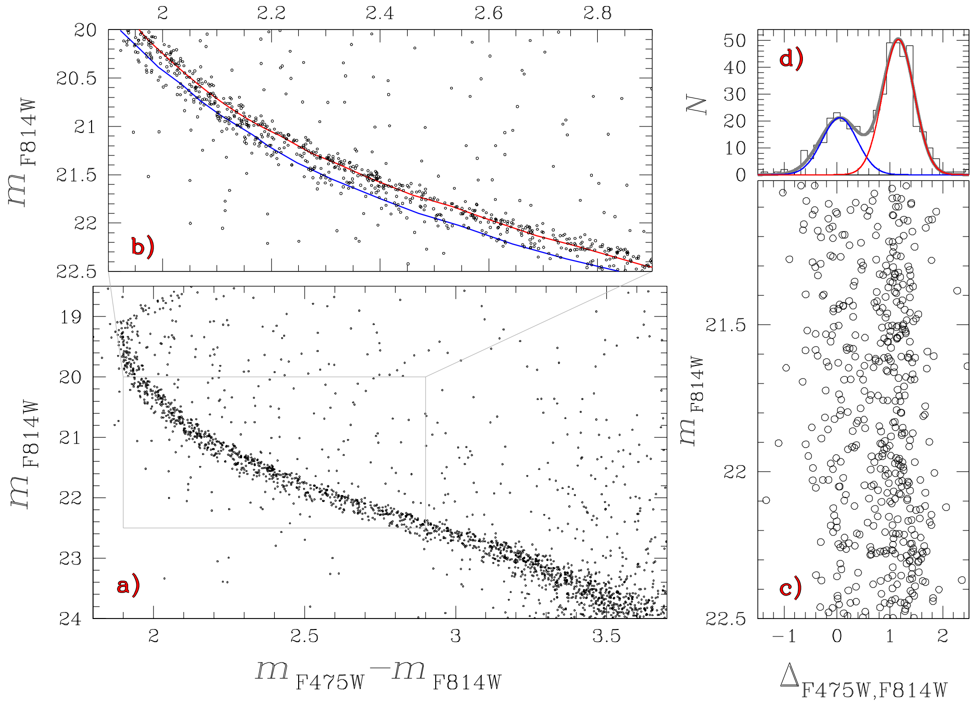

Figure 5. This figure illustrates the procedure to estimate the fraction of blue and red MS stars. Panel (a) shows the $m_{\rm F814W}$ vs. $m_{\rm F475W}-m_{\rm F814W}$ CMD of stars in the parallel field while panel (b) is a zoom-in of stars in the F814W interval where the split MS is more clearly visible. The red and blue lines superimposed on the CMD are the fiducials of the corresponding MSs. A verticalized $m_{\rm F814W}$ vs. $\Delta(m_{\rm F475W}-m_{\rm F814W})$ diagram of the panel (b) stars is shown in panel (c) and the corresponding $\Delta(m_{\rm F475W}-m_{\rm F814W})$ histogram distribution is illustrated in panel (d). The best-fit bi-Gaussian function is superimposed on the histogram (thick gray line) and the two components are colored blue and red.

these color differences with the observed ones by means of χ^2 minimization. The best estimate for the helium content of blue MS stars corresponds to the helium abundance of the isochrone that provides the minimum χ^2 and corresponds to $Y = 0.315 \pm 0.010$. To estimate the uncertainty, we enhanced the color separation between the two MSs by $\pm 1\sigma$, where σ is the error on the color determination, and derived the corresponding helium values by using the procedure above. The uncertainty corresponds to the average of the absolute differences between these helium determinations and the best helium estimate.

The high helium content of the blue MS indicates that it is the counterpart of population $2G_B$, $2G_C$, and $2G_D$ stars. In contrast, $2G_A$ stars have similar helium content to the 1G ($Y \sim 0.25$) and are likely associated with the red MS. These conclusions, based on the chemical compositions of MS and RGB stars, are corroborated by the fact that the fraction of $1G+2G_A$ stars (∼63%) is consistent with the fraction of red MS stars (∼65%).

3.4. Multiple Populations along the HB

To investigate multiple populations along the HB, we exploited the $m_{\rm F275W}$ versus $m_{\rm F275W}-m_{\rm F814W}$ CMD of Figure 7, which is very sensitive to the effective temperature and the luminosity of HB stars. We identified 629 candidate HB stars, including 65 RR Lyrae stars and 27 and 538 stars redder and bluer, respectively, than the RR Lyrae instability strip. The corresponding HB ratio is HBR = 0.81[11] and is higher than that derived by Contreras Peña et al. (2013; HBR = 0.45).

The histogram distribution of $m_{\rm F275W}-m_{\rm F814W}$ of HB stars (bottom panel of Figure 7) is clearly bimodal with a narrow peak centered at $m_{\rm F275W}-m_{\rm F814W} \sim 0.8$ and a much broadened one around $m_{\rm F275W}-m_{\rm F814W} = 3.4$. Both peaks have colors that differ from those of the Grundahl et al. (1999) and Momany et al. (2004) jumps (hereafter the G- and M-jumps), which are located at $m_{\rm F275W}-m_{\rm F814W} \sim 2.4$ and $m_{\rm F275W}-m_{\rm F438W} \sim 1.2$. These jumps are universal features of HB morphology and are due to modifications of the stellar atmospheres (e.g., Brown et al. 2016, 2017). The fact that the two peaks in the HB color distribution appear independent from the G- and M-jumps indicates that they are not related to atmospheric phenomena but can be safely associated with multiple populations.

Although the identification of the five populations of NGC 6402 along the HB is beyond the scope of this paper, we tentatively associated multiple populations along the RGB and the HB as follows. We noticed that 354 out of the 629 HB stars are bluer than $m_{\rm F275W}-m_{\rm F814W} = 2.0$. Hence, about 55% ± 2% of HB stars can be tentatively associated with the red HB peak and the remaining 45% ± 2% with the blue peak. It is tempting to speculate that the red HB peak is composed of 1G and $2G_A$ while the helium-rich populations ($2G_B$, $2G_C$, and possibly $2G_D$) evolve into the blue HB peak. Notice anyway that these fractions of HB stars are slightly but significantly different from the fractions of RGB stars with pristine helium abundances (62% ± 2%) and from the fractions of helium-rich stars (38% ± 2%).

3.4.1. Mass Loss of Multiple Populations

Work based on both theory and high-resolution spectroscopy reveals that the reddest HB tail is composed of the bulk 1G stars, while the bluest portion of the HB is populated by 2G stars with extreme helium content (e.g., D'Antona et al. 2002;

---

[11] The HBR (Lee et al. 1994; Mackey & van den Bergh 2005) is defined as $(B-R)/(B+V+R)$, where B, R, and V are the numbers of stars bluer and redder than the instability strip, and the number of variables in the HB, respectively.

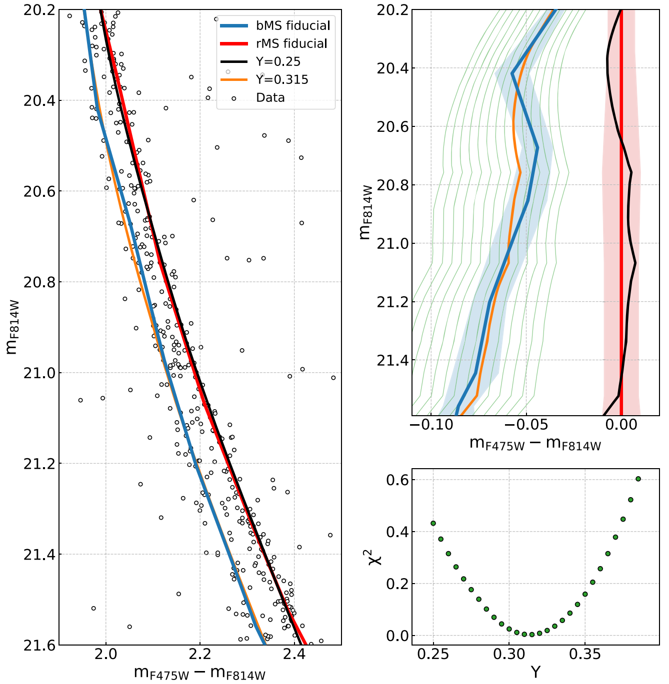

Figure 6. Procedure to estimate the helium abundance of the blue MS in NGC 6402. The left panel shows the $m_{\rm F814W}$ vs. $(m_{\rm F475W} - m_{\rm F814W})$ diagram for MS stars in the parallel field. Red and blue lines represent the fiducials of the red and blue MSs, respectively, while the best-fit isochrones with $Y = 0.25$ and $Y = 0.315$ are colored black and orange, respectively. The upper right panel reproduces the verticalized $m_{\rm F814W}$ vs. $\Delta(m_{\rm F475W} - m_{\rm F814W})$ diagram. Here we added isochrones with Y ranging from $Y = 0.29$ to $Y = 0.36$ in steps of 0.005 (green lines). The shaded blue and red areas enclose the regions within $\pm 1\sigma$ color from the corresponding fiducial. The bottom right panel shows the χ^2 value against the helium abundance of the isochrone used to fit the blue MS. See text for details.

Marino et al. 2011). Based on this evidence Tailo et al. (2019, 2020, 2021) identified 1G stars and 2G stars with extreme chemical composition in 56 Galactic GCs and measured the RGB mass loss. In the following, we extend to NGC 6402 the method introduced by Tailo and collaborators to identify 1G and 2G$_{\rm C}$ stars along the HB and infer their RGB mass losses.

In a nutshell, the method consists of comparing the observed color distributions of the reddest and bluest HB stars with the colors of a grid of synthetic HB stars. Simulated HB stars have different average mass-loss (μ) and mass-loss spread (δ) values. Specifically, μ ranges from 0.200 $M_\odot$ to 0.310 $M_\odot$ in steps of 0.003 $M_\odot$ and δ varies from 0.002 $M_\odot$ to 0.012 $M_\odot$ in steps of 0.001 $M_\odot$.

We assumed for all simulations $[{\rm Fe/H}] = -1.1$, $[\alpha/{\rm Fe}] = 0.3$, and an age of 12.5 Gyr. We adopted $Y = 0.25$ for 1G stars and $Y = 0.315$ for the 2G$_{\rm C}$. Further details on the procedure are provided by Tailo et al. (2020, 2021).

The simulation of 1G stars that provides the best match with the histogram distribution of the reddest HB stars was derived by means of χ^2_d minimization and corresponds to $\mu = 0.240 \pm\ 0.022\, M_\odot$ and $\delta = 0.006 \pm 0.002\, M_\odot$. Similarly, we obtained for 2G$_{\rm C}$ stars $\mu = 0.280 \pm 0.024\, M_\odot$ and $\delta = 0.005 \pm 0.002\ M_\odot$. The results are listed in Table 4 and plotted in Figure 8, where we superimpose the contours of the best-fit synthetic CMDs on the observed CMD (upper panels) and compare the observed and simulated histograms of the colors of 1G and 2G$_{\rm C}$ HB stars.

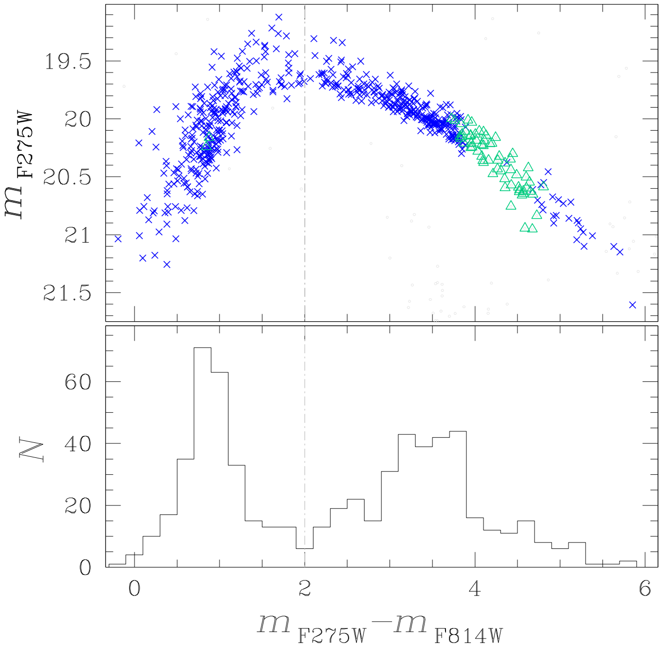

Figure 7. $m_{\rm F275W}$ vs. $m_{\rm F275W} - m_{\rm F814W}$ CMD of HB stars in NGC 6402, with RR Lyrae marked by green triangles (top). The bottom panel shows the histogram color distribution of HB stars. Vertical lines separate the two main groups of HB stars. See text for details.

Table 4
Properties of 1G and 2G$_{\rm E}$ Stars along the HB of NGC 6402

ID	Y	μ ($M_\odot$)	δ ($M_\odot$)	$M_{\rm Tip}$ ($M_\odot$)	$\overline{M}_{\rm HB}$ ($M_\odot$)
1G	0.250	0.240 ± 0.022	0.006 ± 0.002	0.841	0.601 ± 0.022
2G$_{\rm C}$	0.315	0.280 ± 0.024	0.005 ± 0.002	0.757	0.481 ± 0.024

Note. Columns: population ID, helium abundance (Y), average mass loss (μ), mass-loss spread (δ), stellar mass at the tip of the RGB ($M_{\rm Tip}$), and average HB mass ($\bar{M}_{\rm HB}$).

Interestingly, the amount of mass lost by 1G stars in NGC 6402 is comparable with the mass loss of 1G stars in clusters with similar metallicity. Indeed, as shown in the top panel of Figure 9, NGC 6402 follows the same trend in the [Fe/H] versus $\mu_{\rm 1G}$ plane discovered by Tailo et al. (2020, 2021). We also find that the 2G$_{\rm C}$ loses more mass than the 1G, in analogy to what is observed in nearly all other massive GCs. This result is shown in the bottom panel of Figure 9, where NGC 6402 is represented by the purple diamond, and the dots show the extra mass loss $\Delta\mu_e$ in the sample of GCs studied by Tailo et al. (2020).

Actually, the bottom panel of Figure 9 shows that the extra mass loss ($\Delta\mu_e = 0.040 \pm 0.012\, M/M_\odot$) for NGC 6402 is relatively small with respect to that of the other massive clusters. The result depends on the helium content $Y = 0.315$ assumed for 2G$_{\rm C}$ stars: for a smaller value of Y, $\Delta\mu_e$ would be larger and fit better with the trend defined by the bulk of the other clusters. We take this as an indication that $Y = 0.315$ may represent an upper limit to the possible helium content of this extreme population.

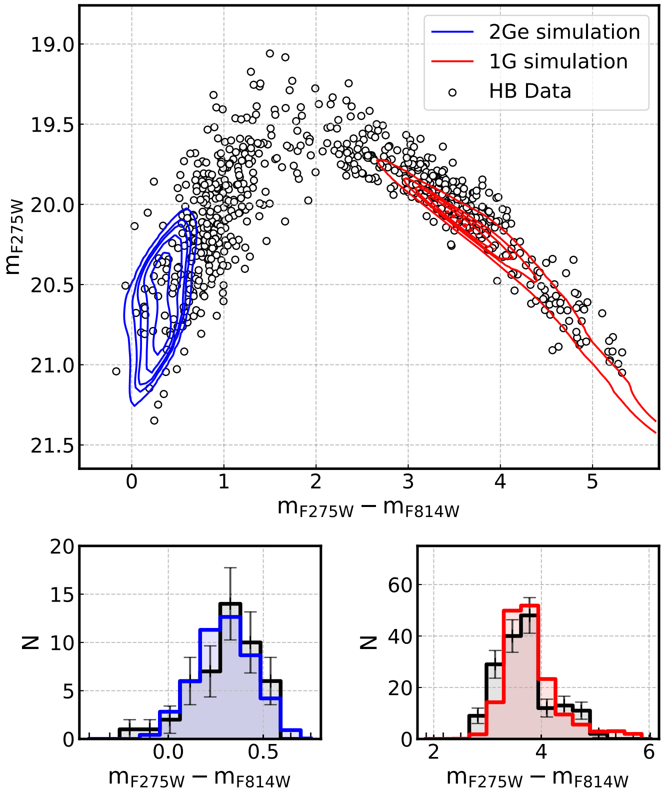

Figure 8. Upper panel: $m_{\rm F275W} - m_{\rm F814W}$ vs. $m_{\rm F275W}$ CMD of the HB stars in NGC 6402. The contour plots represent the best-fit simulation of the 1G and the extreme 2G, respectively, for red and blue. The two bottom panels represent the histograms of the color distributions of observed (black) and simulated stars as direct comparison with the part of the HB where the two simulations overlap in the CMD.

4. Summary on the Fraction of Different Populations from Different Data

Table 5 compares the information gathered on the different populations. The results from the spectroscopic sample in Johnson et al. (2019) are given in the second column. The HST parallel-field data include 65% stars in the red MS and 35% stars in the blue MS. The red MS includes both the P1 and P2 populations. The comparison with the ChM data is quite consistent, if we add together the 1G and $2G_{\rm A}$ data (see Figure 4) and collect as a generic extreme E group all the other populations, including the $2G_{\rm D}$ with probably higher metallicity. In general, we may say that the E group is larger than found in Johnson et al. (2019), a result not so surprising when accounting for the fact that the spectroscopic sample is quite small. The HB data are subdivided into "red" and "blue," at the right and left sides of the color $m_{\rm F275}$–$m_{\rm F814} = 2$ (Figure 7). The resulting fractions are perhaps a bit more surprising, because here we have an even larger (45%) fraction of stars belonging to the blue side of the HB, which should be assigned to the E populations. A possible explanation for the higher percentage of blue HB stars may be that our fraction of red HB stars is too small, as testified by the fact that our RR Lyrae group is much less represented than in Contreras Peña et al. (2018). At first sight, we could attribute the different fraction to the fact that our RR Lyrae sample was obtained at the center of the cluster, while the RR Lyrae stars in the whole catalog are spread all over the cluster: it is plausible that the 1G stars are less concentrated than the 2G stars, as we know to occur in several GCs (see, e.g., Sollima et al. 2007; Bellini et al. 2009; Lardo et al. 2011; Milone et al. 2012c; Simioni et al. 2016; Dalessandro et al. 2019; Dondoglio et al. 2021); Dalessandro et al. (2019) found a spatial segregation of the 2G in about half of a sample of 20 clusters, correlated with the current half-mass relaxation time $t/t_{\rm rh}$. NGC 6402, with an age $t = 12.5$ Gyr derived here and $t_{\rm rh} \sim 2.5 \times 10^9$ yr (Harris 1996), has $t/t_{\rm rh} \sim 5$, in the range where segregation should still be present, and deserves a study of the spatial distribution of the two populations. Anyway, the parallel field is $6'$ far from the cluster center, well out of the central region, but it shows a proportion of 1G+2G mild and 2G extreme stars consistent with those derived from the core data from which the ChM was derived. Thus, further investigation is needed to understand the meaning of the results concerning the HB. We conclude that the HST sample contains about 35% of stars belonging to the extreme and probably also the intermediate populations, while another ~35% of stars belong to the mild 2G.

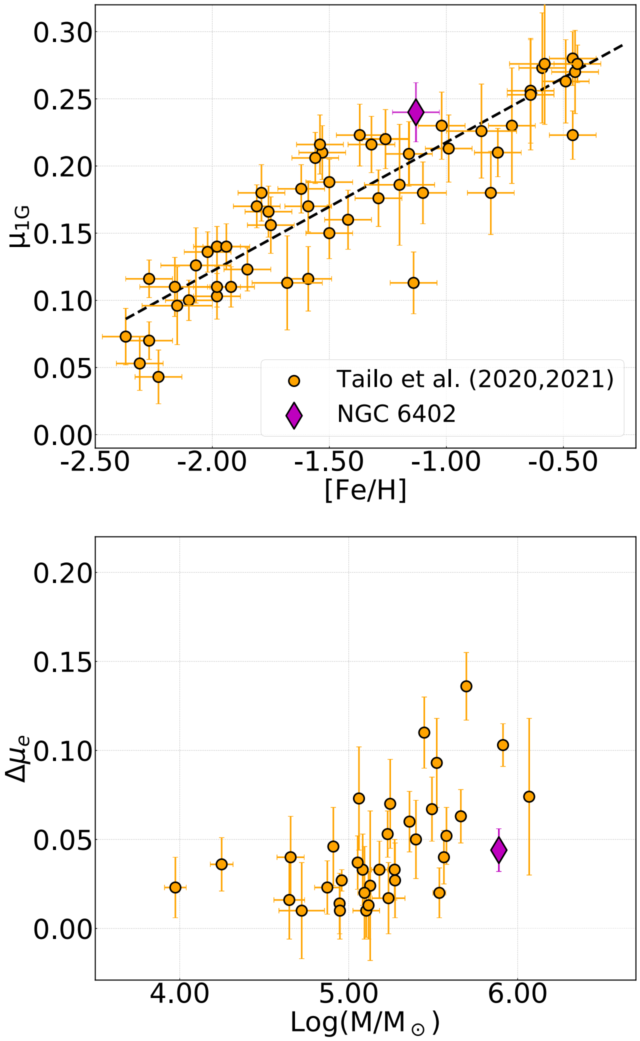

Figure 9. Diagrams of the mass lost during the RGB evolution, $\mu_{\rm 1G}$, vs. [Fe/H] (top) and of the extra mass loss of the 2G, $\Delta\mu_e$, vs. the cluster mass Log($M/M_\odot$) (bottom), from Tailo et al. (2020, 2021). The values of $\mu_{\rm 1G}$ and $\Delta\mu_e$ are in solar masses. NGC 6402 is marked with purple diamonds. The black dashed line in the top panel is the best-fit least-squares straight line of all points.

Table 5
Fractions of Populations in Different Samples

Name	J2019		HST Parallel Field		HST ChM		Tot ChM	HB	
1G	P1	0.34	red MS	0.652	1G	0.280	0.626	red ($m_{\rm F275W} - m_{\rm F814W} > 2$)	0.55
2G mild	P2	0.40			$2G_A$	0.346			
2G extreme	E	0.26	blue MS	0.342	$2G_B$	0.161	0.374	blue ($m_{\rm F275W} - m_{\rm F814W} < 2$)	0.45
					$2G_C$	0.129			
					$2G_D$	0.084			

5. Comparison with NGC 2808

In this section we directly compare the photometric diagrams of NGC 6402 and NGC 2808, which is one of the most studied GCs in the context of stellar populations. Such comparison is possible because NGC 2808 and NGC 6402 have similar metallicities, ages, and masses.

NGC 2808 hosts populations with extreme contents of helium and light elements that have been investigated along various evolutionary sequences, including the MS, the RGB, the HB, and even the AGB (e.g., D'Antona et al. 2005; Piotto et al. 2007; Carretta et al. 2009; Marino et al. 2014, 2017; Lagioia et al. 2021). In the following, we discuss multiple populations in NGC 2808 along the RGB stars, the MS, and the HB by using the same photometric diagrams available for NGC 6402.

As illustrated in the left panel of Figure 10, the ChM of NGC 2808 reveals that both 1G and 2G stars are not chemically homogeneous. The 1G stars host two main stellar populations (namely A and B), whereas the 2G is composed of at least three distinct groups of stars (C, D, and E). The 1G stars share pristine helium abundance ($Y \sim 0.25$) and light-element abundances but are possibly inhomogeneous in metallicity, with population A stars being slightly more metal-rich than population B stars. In contrast, 2G stars are enhanced in He, N, and Na and depleted in C and O. Specifically, population C stars may be very slightly enriched, by ~0.005 dex in helium mass fractions (D'Antona et al. 2016), while population D and E stars have larger helium contents up to $Y \sim 0.29$ and $Y \sim 0.35$, respectively.

NGC 2808 exhibits an extended HB that is well populated on both sides of the RR Lyrae instability strip. The $C_{\rm F275W,F336W,F438W}$ versus $m_{\rm F275W} - m_{\rm F814W}$ diagram of HB stars is plotted in the middle panel of Figure 10, where we mark the position of the G- and M-jumps. Work based on high-resolution spectroscopy and on simulated HBs shows that the red HB hosts stars with different sodium contents but similar helium abundances. Hence, it is composed of population A, B, and C stars (e.g., Marino et al. 2014; D'Antona et al. 2016). Population E stars mostly evolve into the bluest HB tail, on the hot side on the M-jump. The HB region between RR Lyrae and the M-jump is mainly composed of population D stars.

CMDs made with optical filters did not allow us to disentangle the five stellar populations of NGC 2808. Nevertheless, the $m_{\rm F814W}$ versus $m_{\rm F475W} - m_{\rm F814W}$ CMD plotted in the right panel of Figure 10 reveals a triple MS. In this diagram, the red MS is composed of stars of populations A, B, and C and is reproduced by isochrones with nearly pristine helium content. The middle and the blue MS correspond to population D and population E stars, respectively. According to Milone et al. (2012b), the three MS populations contain the following fractions of stars: 0.62 ± 0.02 (red MS), 0.24 ± 0.02 (middle MS), and 0.14 ± 0.03 (blue MS).

The comparison between NGC 2808 and NGC 6402 is illustrated in Figure 11. In the upper left panel we superimpose their $\Delta_{C\rm F275W,F336W,F438W}$ versus $\Delta_{\rm F275W-F814W}$ ChMs in such a way that the 1G stars of both clusters share the same median values.

Clearly, the ChM of NGC 6402 is significantly less extended in both axes with respect to the NGC 2808 map. In particular, there is no evidence for NGC 6402 counterparts of the most helium-rich stars of NGC 2808 (population E). We also find that the 1G stars of NGC 6402 roughly match population B of NGC 2808, while there is no evidence for population A–like stars. The group of $2G_A$ stars of NGC 6402 mostly overlaps population C of NGC 2808 and the similarity between these populations is corroborated by their chemical compositions. Indeed, both the $2G_A$ stars of NGC 6402 and the population C stars of NGC 2808 have similar He and O content to the 1G but are significantly enhanced in nitrogen. Populations $2G_B$ and $2G_C$ are analogs of population D stars in NGC 2808, as demonstrated by the location on the ChM and the helium content $Y \sim 0.30$. Intriguingly, NGC 2808 lacks a counterpart for the $2G_D$ stars. These results are confirmed from the comparison of the $\Delta_{\rm F336W-F438W}$ versus $\Delta_{\rm F275W-F814W}$ ChMs of NGC 2808 and NGC 6402 plotted in the bottom left panel of Figure 11.

The lack of stars with extreme helium content in NGC 6402 is corroborated by the comparison of the $m_{\rm F814W}$ versus $m_{\rm F475W} - m_{\rm F814W}$ CMDs (bottom left panel). Clearly, the red and middle MSs of NGC 2808 match the red and blue MSs of NGC 6402, whereas NGC 6402 does not host a counterpart for the blue MS (i.e., population E) in NGC 2808. As expected, when we superimposed on the CMD the isochrones with different helium contents that reproduce the triple MS of NGC 2808, the result was that the blue MS stars of NGC 6402 are not consistent with the most helium-rich isochrone ($Y = 0.36$).

The comparison of the HBs of the two clusters is plotted in the upper right panel of Figure 11. Clearly, the HB stars of both clusters follow the same sequence in the $C_{\rm F275W,F336W,F438W}$ versus $m_{\rm F275W} - m_{\rm F814W}$ plane (see Brown et al. 2016 for details). The HB of NGC 6402 exhibits a shorter $m_{\rm F275W} - m_{\rm F814W}$ color extension as compared to NGC 2808 and shows no evidence for blue-hook stars, which are the progeny of stars highly enhanced in helium. These facts corroborate the evidence that NGC 6402 does not host stars with extreme helium content. In contrast to NGC 2808, NGC 6402 does not show a red HB; thus NGC 6402 is a second-parameter cluster belonging to the M13 group. For a recent discussion of this problem see Tailo et al. (2020) and references therein. Since the reddest HB tail is mostly populated by 1G stars, we expect, in addition to metallicity, at least one second parameter is responsible for the color of the 1G stars. Age

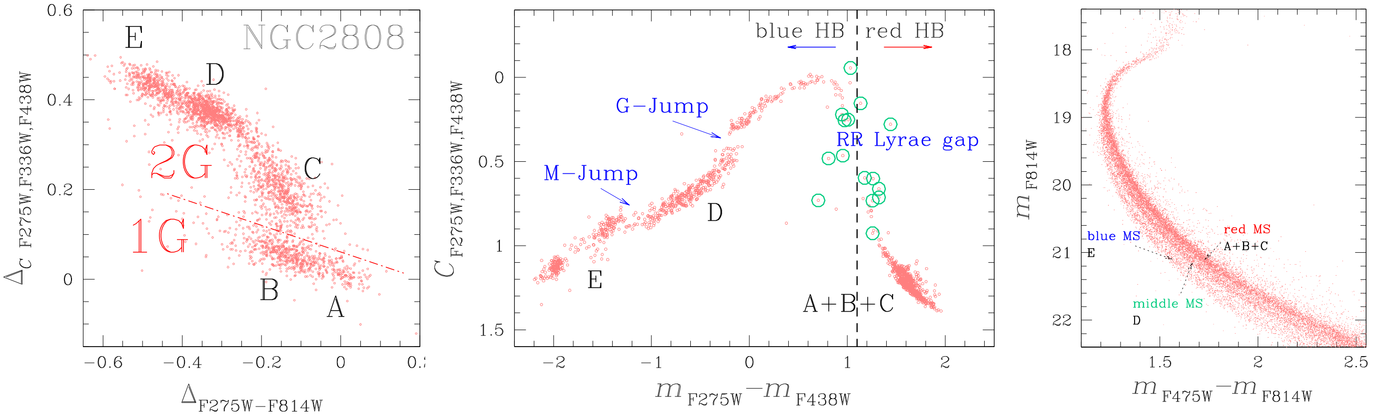

Figure 10. Left: ChM of RGB stars in NGC 2808. The red dashed–dotted line separates the bulk of 1G stars from the 2G. Middle: $C_{F275W,F336W,F438W}$ vs. $m_{F275W}-m_{F814W}$ diagram of HB stars in NGC 2808. Candidate RR Lyrae stars are marked with green circles. The vertical dashed line separates the red and the blue HB. We indicate the position of the M- and G-jumps and the gap associated with the RR Lyrae instability strip. Right: Optical, m_{F814W} vs. $m_{F475W}-m_{F814W}$, CMD of NGC 2808 stars zoomed in on the MS and the SGB. The red, middle, and blue MSs are indicated by the black arrows. The letters A–E in all panels indicate the five main populations of NGC 2808.

differences as well as mass-loss differences are possible second parameters. As an alternative, stars on the red HB tail of NGC 6402 should be more helium-rich than the red HB stars of NGC 2808 (D'Antona & Caloi 2008).

6. A Summary of Models

The issue of multiple populations includes chemical "anomalies" of quite a number of elements, with different problems highlighted by different stars in different clusters. For some of these anomalies the contribution of some particular polluters may be required.[12] Nevertheless, most of the scenarios proposed to explain light-element variations do not withstand a general scrutiny. We refer the reader to the complete summaries available in the recent literature (e.g., Renzini et al. 2015; Bastian & Lardo 2018; Gratton et al. 2019) and discuss here the only two remaining models that at least basically conform to the requirements of the chemistry displayed in massive clusters, such as NGC 2808 and NGC 6402, containing an "extreme" population. These are the SMS model, here considered in the basic formulation by Denissenkov & Hartwick (2014) and Denissenkov et al. (2015) that also includes a qualitative description in terms of a dynamical scenario (Gieles et al. 2018), and the AGB model (Ventura et al. 2001). In AGB stars the hot environment where light elements are processed by proton captures is not the stellar core, but the burning at the "hot bottom" of the convective envelope (HBB), from where the elements are then transported by convection in the whole envelope and then lost by stellar wind and planetary nebula ejection.

For the present work, the models are considered mainly to understand whether the ejecta composition (with or without dilution with pristine gas) is compatible both with the patterns of light-element abundances in the giants (Johnson et al. 2019) and with the helium content derived here for NGC 6402. At the end of our analysis, we will conclude that neither model in its present stage of development is compatible with the helium abundance of the extreme 2G, and suggest possible additional formation mechanisms.

6.1. The SMS Model

The reason to propose that SMSs of about $10^4\ M_\odot$ are at the origin of the elemental abundances found in the second population of GCs, although the highest mass that can be formed by simple fragmentation is 100 times smaller, is that such structures achieve the central temperature of ∼75 MK, necessary to allow the reaction ^{24}Mg(p,γ)^{25}Al, which depleted ^{24}Mg in the gas forming the extreme GC stars. This temperature is not reached in the cores of standard massive stars. Another advantage is that p-captures by Mg isotopes in SMS cores produce isotopic ratios compatible with the ratios observed in five clusters (Da Costa et al. 2013), while discrepant ratios are found when these reactions occur in the AGB HBB environment (Ventura & D'Antona 2009).[13] Difficulties remain in explaining the production of silicon by p-captures on aluminum—a Si–Mg anticorrelation is present in NGC 2808 giants (Carretta 2015)—as Si production occurs at the expense of the total depletion of Mg and Na in the cores of SMSs; further, potassium cannot be produced (Prantzos et al. 2017). Nevertheless, the SMS model also provides an advantage in the description of oxygen depletion and sodium enhancement (see in Section 6.2 the difficulties of the AGB model) as shown in the case of M13 by Denissenkov et al. (2015), whose $60 \times 10^3\ M_\odot$ model chemistry at $Y_{\rm core} = 0.38$, diluted by 50% with pristine gas, is able to reproduce the abundance patterns of O–Na and the isotopic Mg ratios.

Notice that for these same O–Na abundances, a small dilution by ∼10% with pristine matter brings them in the correct range to describe the E stars in NGC 6402.

A further interesting feature of the SMS model is that it could help solve the "uniqueness" problem of extreme-composition stars being found only in a few very massive

---

[12] For instance, the s-process elemental distribution in the metal-poor star ROA 276 in ω Cen (Yong et al. 2017) is well explained by the rotating models by Frischknecht et al. (2012, 2016).

[13] The correct isotopic ratios for magnesium can be obtained in the AGB models by enhancing by a factor ∼3 the proton capture rate by ^{25}Mg at temperatures ∼100 MK, particularly by the ^{25}Mg(p,γ)^{26}Al^{m} channel, beyond the most recent experimental determinations (Ventura et al. 2018). With this input, the AGB nucleosynthesis also correctly predicts the total Mg depletion in different clusters, and its trend with the metallicity. Larger Mg depletions are observed in clusters of lower metallicity (e.g., Mg is reduced by a factor ∼10 in the cluster NGC 2419; Cohen & Kirby 2012). This trend is an observational constraint not directly predictable in the case of SMSs, as the temperature at which nuclear activity takes place in the central regions is almost unaffected by the metallicity, unlike the HBB conditions in massive AGB stars.

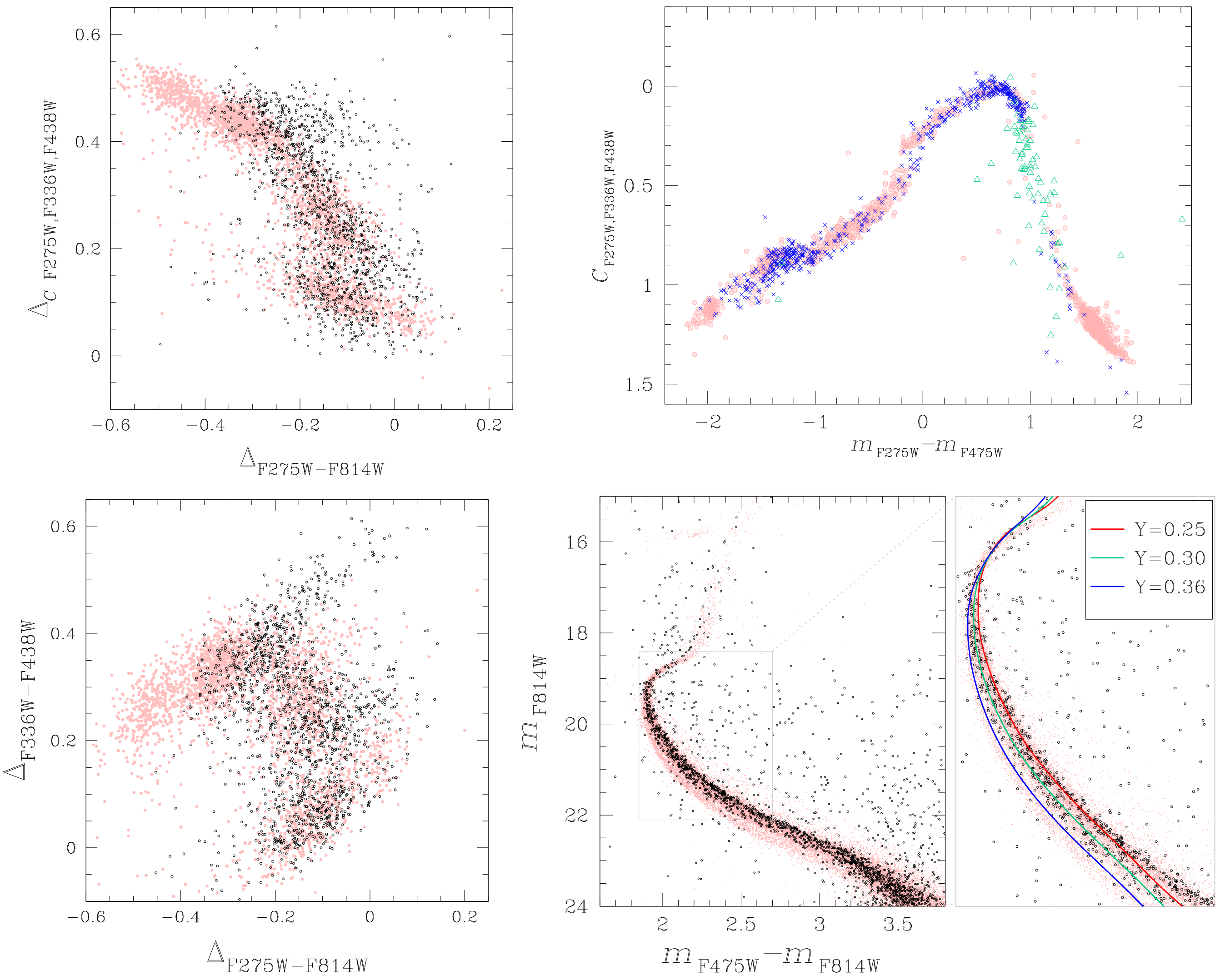

Figure 11. Upper panels: Comparison of the $\Delta_{CF275W,F336W,F438W}$ vs. $\Delta_{F275W-F814W}$ (upper left) and $\Delta_{F336W-F438W}$ vs. $\Delta_{F275W-F814W}$ ChMs (lower left) of NGC 2808 (pink points) and NGC 6402 (black points). The right panels compare the HBs of NGC 2808 (pink) and NGC 6402 (same colors as in Figure 1; top) and the m_{F814W} vs. $m_{F475W} - m_{F814W}$ CMDs (bottom). We also provide a zoomed-in image of the CMD on the upper MS, where we compare the observations of NGC 2808 and NGC 6402 with isochrones with different helium abundances. See text for details.

old GCs, because only those have the opportunity to host and evolve SMSs (see in Section 6.2 the alternative view of the AGB model).

Going beyond the nucleosynthesis results, we must remark that the possible successes of the SMS site for nucleosynthesis of multiple populations have strong constraints, as follows:

1. The protocluster must be able to form SMSs of a required mass of $\sim 2\text{–}10 \times 10^3\,M_\odot$ (Denissenkov & Hartwick 2014; Prantzos et al. 2017). First, massive stars must sink to the cluster core due to dynamical friction and then merge by multiple collisions. Models aimed at explaining the possible presence of intermediate-mass black holes in young massive clusters have been developed (Portegies Zwart et al. 1999, 2004). The process is constrained to occur within the very short MS timescale of such objects.
2. The core H-burning (MS) must be stopped very early, and at the specific time required to avoid the condition that the SMS ejecta have helium content higher than the maximum helium observed in the extreme GC populations, roughly constrained to be always $Y < 0.4$. The hypothesis is that SMSs lose at early times a great fraction of their mass, as a result of some instabilities and stellar winds. No quantitative models are still available to support these suggestions. The ejecta then mix with the gas of the environment and form the second-population stars, showing different degrees of p-capture processing.

For the purpose of this work, we put aside these problems, and keep the chemistry of the diluted SMS gas as the basis for the formation of the E population in NGC 6402, as depicted in Johnson et al. (2019). Note anyway that the E population includes about 26% of the cluster mass, $\sim 3.5 \times 10^5\,M_\odot$ if we refer to a present mass of $1.4 \times 10^6\,M_\odot$. Assuming now a dilution of ∼40% with pristine gas, we need anyway to process within an SMS mass $\sim 2 \times 10^5\,M_\odot$. Thus, either 20 SMSs of $10^4\,M_\odot$ each, or a model such as the "conveyor belt" proposed by Gieles et al. (2018) is necessary to achieve such a result. We must therefore consider that there are still many unexplored aspects in the model.

6.2. The AGB Model

The AGB model attributes the chemistry of multiple generations to star formation in the gas expelled at low velocities by massive AGB and super-AGB stars, collected into the central regions of the cluster and possibly diluted with residual or reaccreted pristine gas.

From the point of view of the chemistry of the different multiple populations, D'Antona et al. (2016) have developed the idea that the populations are the result of formation along the "timeline" of evolution of the different super-AGB and AGB masses, having different ejecta composition. Application to the prototype cluster NGC 2808 showed that the populations A, B, C, D, and E by Milone et al. (2015) should have formed in the order B E D C A. At first, the standard population B forms; then the extreme population E, *undiluted*, at the time of evolution of the masses that undergo super-AGB evolution; then the intermediate population D, partially diluted with pristine gas; and then population C, very diluted with pristine gas and thus showing only very mild differences with respect to the standard B. The last population A was suggested to be polluted by the ejecta of some Type Ia supernovae (SN Ia), whose regular explosions eventually expel the reaccreting pristine gas and end the second star formation epoch. Of course the details of the evolution of each cluster determine the variety of chemical patterns found among different clusters. In particular, the E population, whose chemistry indicates that it forms *before* reaccretion, can be present only in clusters in which the reaccretion of pristine gas is delayed enough, and models show that these are the most massive clusters only (D'Ercole et al. 2016), in agreement with observations (e.g., Figure 13 in Milone et al. 2018).

Concomitantly, the helium content of the E populations must be equal to the abundance in the pure ejecta of these stars, and all models agree that, for general structural reasons, this must be in the range $Y = 0.34$–0.38 (Ventura 2010). Note that this prediction is confirmed by the indirect derivation of helium content in the blue MS of ω Cen (e.g., Tailo et al. 2016) and NGC 2808 (D'Antona & Caloi 2008) and it is one of the successes of the AGB model: while the SMS model *has to require* that the MS evolution stops at a very specific time, so that the average helium after dilution is close to that required by observations, the AGB model predicts this limit.

Another straightforward prediction of the AGB model is that nucleosynthesis, for the same degree of dilution, should be more advanced in clusters of lower metallicity (Ventura et al. 2013). Lower amounts of metals imply lower opacities in the AGB envelopes, and a higher temperature at the basis of the envelope where p-capture nucleosynthesis takes place. In particular, at higher metallicity the ON chain and p-captures on Mg isotopes are less efficient. This naturally produces the "vertical" Na–O relations of the bulge clusters having the largest GC metals (Muñoz et al. 2020, and references therein).

In this work, our attention must anyway consider the crucial issue not fully solved in the models, namely the oxygen and sodium yields. A thorough discussion is given in Renzini et al. (2015), and can be summarized by saying that, in the range of the HBB temperatures of massive AGBs, the p-captures on sodium destroy it, while at the same time p-captures on oxygen nuclei convert them to nitrogen. The interplay between these two concomitant reactions is such that sodium is depleted, if the star lives long enough to pursue a strong oxygen depletion. Thus, strong mass loss (as in the super-AGBs) preserves sodium, but does not destroy enough oxygen, while lower rates of mass loss (as in the massive AGBs) can deplete more oxygen, but preserve less sodium. The resulting O–Na relation is shown by the (red) hook line in Figure 12. The yields shown as red squares are from the extension of the work by Ventura et al. (2013) to a metal mass fraction $Z = 1.5 \times 10^{-3}$ ([Fe/H] ~ -1.3) (Dell'Agli et al. 2018) close to the metallicity of both NGC 2808 and NGC 6402. The upper right red square results from the evolution of 7 $M_\odot$; smaller masses follow until the 5 $M_\odot$ model, which is the mass of maximum oxygen depletion; and the 4.5 $M_\odot$ model again displays larger sodium and oxygen abundances in the ejecta.

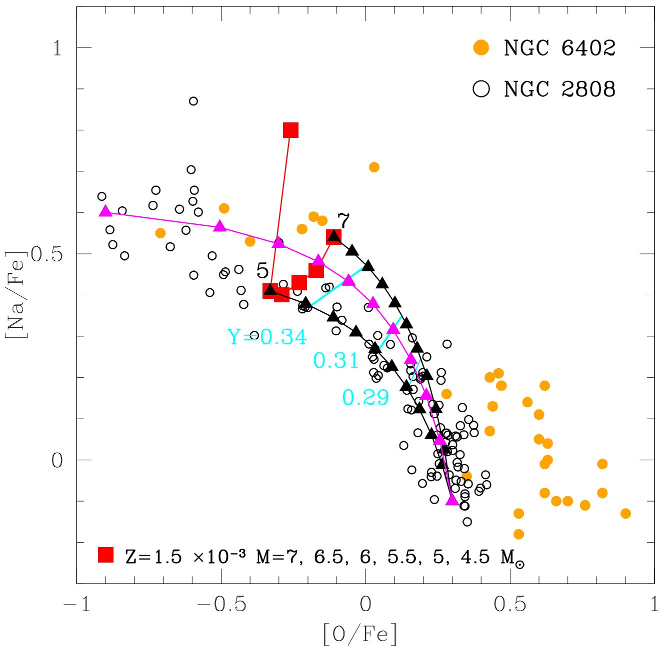

Figure 12. The Na–O data for NGC 2808 (black open circles) and for NGC 6402 (orange dots) are shown together with the average Na–O content in the ejecta of AGBs and super-AGBs having $Z = 1.5 \times 10^{-3}$ shown as red squares. The top right square refers to 7 $M_\odot$, and the last square on the left represents the abundances in the 4.5 $M_\odot$ ejecta. The black lines with triangles represent the abundances obtained by diluting the ejecta of 7 $M_\odot$ and of 5 $M_\odot$ with increasing amounts of a pristine gas having the abundance [Na/Fe] $= -0.15$ and [O/Fe] $= 0.3$. Actually oxygen in the 1G of NGC 6402 looks much larger on average, with respect to the Carretta (2015) determination of the 1G values in NGC 2808 and in many other clusters (Carretta et al. 2009). The violet line with triangles defines an empirical dilution line starting at [O/Fe] $= -0.9$ and [Na/Fe] $= 0.6$. The diagonal cyan lines show the helium content along the dilution lines—see text.

The yields in the range 5–7 $M_\odot$ are close enough to the cooler points of the E group in Johnson et al. (2019). The three most oxygen-depleted giants ([O/Fe] $\lesssim -0.4$) are out of the curves, as well as the E stars in NGC 2808. In the context of the AGB model, an additional oxygen reduction is attributed (D'Ercole et al. 2012; D'Antona et al. 2016) to anomalous "deep mixing" in giants (D'Antona & Ventura 2007), active when a high helium content reduces the discontinuity in the hydrogen profile left by the maximum deepening of convection at the first dredge-up. Notice that this interpretation *requires* that these stars be born with a high helium content, such as the maximum helium yield of the massive AGB and super-AGB evolution discussed above.

In summary, yields are reasonable for stars of the E group with lower O depletion, but require an additional hypothesis to describe the three most extreme giants, according to today's state of the art.

6.3. A Mixed Model

As discussed above, only SMS and AGB stars reach temperatures high enough to account for the chemical composition of 2G extreme stars, even with the mentioned uncertainties. In addition, other dynamical events may concur to determine the present-day stellar content of NGC 6402. In particular we can consider whether the cluster is the result of the merging of different clusters (e.g., Sugimoto & Makino 1989; van den Bergh 1996; Amaro-Seoane et al. 2013). Searle & Zinn (1978) were the first to argue that some fraction of Galactic GCs have an external origin, and that the outer halo GC system is due to the merger and accretion of "protogalactic fragments"[14] and Searle (1977) even argued that merging of clusters could be possible within these fragments. Mergings occurring in the Galactic thick disk are modeled today (e.g., Khoperskov et al. 2018); they may be relevant to understanding the difference in metallicity and the difference in age by many gigayears between the two populations of the bulge clusters Terzan 5 (Ferraro et al. 2016) and Liller 1 (Ferraro et al. 2021). Cluster mergers have also been explored as a possible solution to the existence of iron-complex clusters as well (e.g., Gavagnin et al. 2016).

In the case of NGC 6402, there are two aspects for which it is useful to consider the merging hypothesis:

(1) If the 2G extreme stars are manufactured by the SMS ejecta in one cluster and the 2G mild stars are born from AGB polluted gas in another one, the presence of the gap in abundances has a simple solution; this may help address the primary SMS problem that very high stellar masses are required (see Section 6.1).

(2) Merging could explain the presence of a small fraction of (likely) metal-richer stars identified in the ChM (group $2G_D$).

7. Discussion

Taken at face value, the high-dispersion spectrum observations give partially contradictory results about how extreme the E composition stars are in NGC 6402. Magnesium abundances are reduced at most by ∼0.2 dex (see Figure 8 in Johnson et al. 2019), to be compared with the ∼0.5 dex of the E stars in NGC 2808 (Carretta 2015), so we should conclude that the E stars in NGC 6402 are not as extreme as those in NGC 2808.

On the other hand, the oxygen abundances in the E sample of both clusters have formally a similar logarithmic depletion (by ∼1.2 dex) with respect to the 1G (or P1) abundances, indicating a similarly "extreme" nuclear processing. This result, anyway, is mostly due to the large difference between the $[\mathrm{O/Fe}]_{1G} \sim 0.3$ of NGC 2808 (Carretta et al. 2009; Carretta 2015), and the $[\mathrm{O/Fe}]_{1G} \sim 0.6$ of NGC 6402 (Johnson et al. 2019)—see Figure 12. The zero-point of the 1G is very important for the depletion models, as the ON cycle depletes oxygen in proportion to its initial content, so that, in a first approximation, stellar models having the same physical conditions (e.g., HBB temperature) but different initial oxygen abundances have about the same logarithmic decrease in oxygen.

These contrasting results, together with the result of the present work, lead us to assume, for the present analysis, that there is a zero-point difference between the 1G abundances by Carretta (2015) and by Johnson et al. (2019), and that we can discuss the depletion of oxygen in NGC 6402 assuming that its 1G abundance is a bare $[\mathrm{O/Fe}] \simeq 0.3$. With this assumption, the E stars in NGC 6402 are not oxygen-depleted as much as those in NGC 2808.

7.1. Helium in the Extreme Population of NGC 6402

The present work shows that the multiple populations hosted in NGC 6402 are not as extreme as the multiple populations in the prototype cluster NGC 2808. Three direct comparisons—simplified by the very similar metallicities of the two clusters—show this:

1. The ChM of NGC 6402 does not contain stars in the location of the E group in NGC 2808 (Milone et al. 2015; see Section 3).
2. The comparison of the CMDs of the two clusters shows that the blue MS of NGC 2808, identified with a population having $Y \sim 0.35$–0.38 (D'Antona et al. 2005; Piotto et al. 2007), is much bluer than the extreme MS in NGC 6402, which can be fit with $Y \sim 0.31$ (see Section 3.4.1).
3. The HB of NGC 6402 does not include the well-populated blue hook, generally modeled as the site of post-RGB evolution of the high-helium population (D'Antona & Caloi 2004; Lee et al. 2005; D'Antona & Caloi 2008; Tailo et al. 2015). If the reddest HB is modeled by assuming that it is populated by 1G stars with $Y = 0.25$, the extreme HB can be fitted with stars having $Y = 0.31$. Consideration of the extra mass loss needed to fit 2G HB stars (Tailo et al. 2020) shows that this value $Y = 0.31$ may be an upper limit to the helium content of hot HB stars (see Section 3.4.1).

We first investigate whether the AGB model and the SMS model are in qualitative or quantitative agreement with this result.

The conclusions inferred in the context of the AGB scenario are illustrated in Figure 12: the three cyan lines mark the O–Na locus where the dilution provides a helium abundance of $Y = 0.34$, 0.31, and 0.29. It is clear that only gas diluted with 40%–50% of pristine gas has $Y = 0.31$, and consequently its O abundance is much larger than that in the E stars of NGC 6402, and vice versa for the Na abundance. The E stars' oxygen is reproduced only by undiluted models (at $Y \sim 0.35$), or by models assuming deep extra mixing, which, anyway, also requires a similarly high initial helium (D'Antona & Ventura 2007). Further, the $Y = 0.31$ locus is in the middle of the O–Na region, where there is a gap in the Johnson et al. (2019) data.

In order to obtain consistency with the data, we need a much stronger O depletion in the yields (such as those obtained for lower metallicity) but one preserving the sodium. This problem has never been solved in the models (Renzini et al. 2015; D'Antona et al. 2016) and brings us back to a key point of discrepancy in the AGB model.

For the SMS model, based on the results shown by Denissenkov et al. (2015) for M13 (their Figure 1 and Table 1), the location of giants with [O/Fe] in the range −0.5 to −0.1 is obtained by dilution with 10%–20% of pristine gas, from pure ejecta having $Y = 0.384$. Then, also in this case these stars should have $Y = 0.357$–0.37. We cannot exclude the possibility

---

[14] Today this hypothesis has a part in the cosmological context of hierarchical structure formation (e.g., Forbes et al. 2018).

that there could be a combination of fine-tuned SMS conditions (central temperature of H-burning (or SMS mass), helium core abundance at the stop of the core evolution, and gas shedding) that allows a lower helium content concomitant with the O–Na abundances of the E population. Ad hoc computation of nucleosynthesis such as those presented in Prantzos et al. (2017) could be useful for exploring the range of parameters and clarifying whether the "mixed" SMS+AGB model by Johnson et al. (2019) can be considered feasible from the helium point of view.

7.2. Helium and the Oxygen and Nitrogen Abundances: What Is Required from Models

Figure 13 shows what is needed by a successful model to conform to the results obtained from the analysis of NGC 6402 HST data. Whatever the model (a modified AGB or SMS model) the ejecta of at least some of the stars must have a very low oxygen abundance (say ∼5% of the pristine one), and a reasonably large sodium abundance (e.g., [Na/Fe] = 0.55, as chosen in the figure), but, also, a helium abundance not exceeding $Y \sim 0.35$ (as found in massive AGBs). Only in this case is it possible to have a helium abundance of ∼0.315 by diluting with pristine gas, and still reproduce the location in the O–Na plane of the bulk of the E stars in the Johnson et al. (2019) sample, as shown in the top panel.

New modeling is needed to understand whether the chemistry of the ejecta of super-AGB and AGB stars and SMSs can be made compatible with this requirement.

The bottom right panel of Figure 13 shows instead the plausible run of nitrogen in the same ideal model. Indeed, if oxygen is reduced to 1/20 in the processing, more oxygen has been processed to nitrogen and the ejecta reach a value of [N/Fe] ∼ 1.8, to be compared to the value of ∼1.3 corresponding to a reduction of δ[O/Fe] ∼ 0.4. This has an interesting consequence on our understanding of the HST results, as we show in the next section.

7.3. The ChM and the "Lack" of an Intermediate Population

A comparison between the ChM of NGC 6402 (black) and the ChM of NGC 2808 (red) is shown in Figure 11, and highlights how powerful photometry can be at providing a complementary vision to the high-dispersion spectroscopic results. The large gaps in [O/Fe], [Na/Fe], and [Al/Fe] distributions found in the spectra suggest that at most 10% of the total population is contained in the "intermediate" range (the I (or D) population). This is in partial agreement with the UV photometry, as the ChM shows overdensities for the E group and for stars closer to the first population. In the D'Antona et al. (2016) scheme for the timing of formation of different multiple populations, the gap in abundances is obtained if, after the formation of the moderately diluted 2G extreme E star group, reaccretion of pristine gas is fast enough that the late-forming stars belong to the very diluted P2 (or 2G mild) group. On the other hand, Johnson et al. (2019) interpret the gap as a possible evidence of delayed formation for intermediate-composition stars. Thus the birth of the second population would consist of two distinct phases, an early one to form the 2G extreme stars, and a very late one to form the P2 (or 2G mild) stars, and suggests the possibility that there are two different classes of polluters. The merging of two clusters with very close initial abundances would provide a natural site for this occurrence.

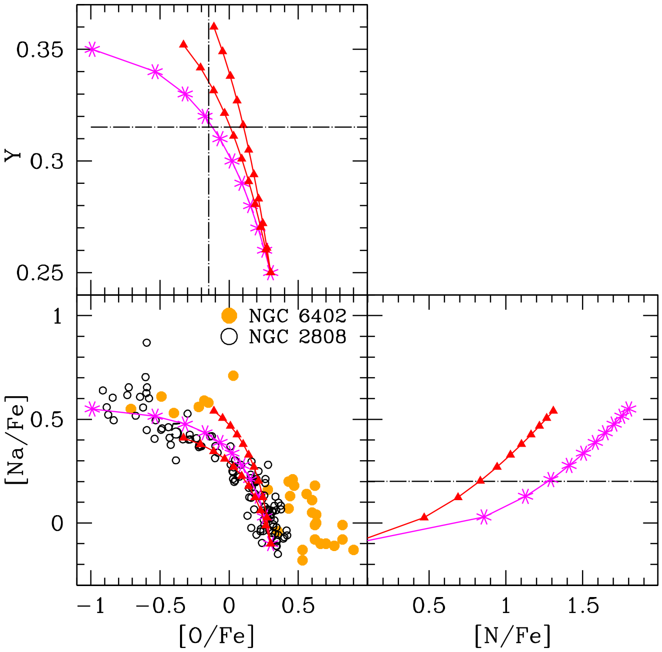

Figure 13. The bottom left panel shows the Na–O data for NGC 2808 and for NGC 6402 together with the dilution curves of the models (see the caption of Figure 12) and an ideal dilution curve (magenta line with stars) starting at [O/Fe] = −1.0 and [Na/Fe] = 0.55. The top panel shows the helium content along the dilution curves as a function of [O/Fe] and the right bottom panel shows the [N/Fe] abundance along the dilution curve. The [N/Fe] of the ejecta having [O/Fe] = −1 in this context is roughly 1.8, 0.6 dex larger than the [N/Fe] of the model of 5 $M_\odot$ used as a comparison.

7.4. Group 2G$_{\rm D}$

The ChM in Figure 3 and its comparison with NGC 2808 in the upper left panel of Figure 11 show clearly that the extreme 2G in NGC 2808 extends beyond the extreme 2G of NGC 6402. At the same time, they show that NGC 6402 includes a group of stars that are typical of Type II or iron-complex clusters. Lacking spectroscopic evidence, we can speculate that ∼9% of the cluster stars are enriched in metals. Notice that they are 2G stars, without a clear 1G counterpart. Also NGC 2808 possibly hosts stars with higher metallicity (group A in Figure 11) but, in contrast, they belong to the 1G. This must be telling us something about the pollution mechanism. In the D'Antona et al. (2016) model, the higher-metallicity groups are born from gas contaminated by the first SN Ia explosions, before these explosions fully expel the gas out of the GC putting an end to 2G star formation. The timing of this event helps to explain why iron-richer groups are often s-process rich, being polluted by the ejecta of AGBs of smaller mass, where s-process enhancements are due to prolonged third dredge-up phases. In the case of NGC 6402, the SN Ia pollution must have occurred mainly on p-processed gas, while pollution took place within a pristine gas region in NGC 2808.

As the 2G$_{\rm D}$ group is mainly 2G, it is unlikely that it is a signature of merging. Further speculation is beyond the scope of this work. The results presented here for NGC 6402 call for additional efforts in the development of new theoretical models.

7.5. The Lack of a Gap in the ChM

We remark here that the lack of a "gap" in the ChM is not in contradiction with a possible gap in some of the light-element abundances, because the ordinate in the ChM mostly traces *the nitrogen abundance*, which can be more continuous than Na or Al, if the p-processed gas comes from progenitors having different nucleosynthesis patterns. From Figure 13, if there are indeed yields as low in oxygen to justify the low value of $Y = 0.315$ for the E population, necessarily their nitrogen abundance in the ejecta is much higher, up to a factor 2.5 (or 0.4 in the log) larger than the nitrogen in ejecta that deplete less oxygen, such as in the 5–7 $M_\odot$ AGB models. The right bottom panel of Figure 13 shows then that stars with similar sodium abundances (e.g.,[Na/Fe] = 0.2) may differ by up to 0.5 dex in nitrogen. Thus the evolution of stars with intermediate oxygen depletion (and different nitrogen) may result in a continuous coverage of the ChM. Spectroscopy of stars in the less populated region of the ChM would be very useful, because it can help to discriminate between stars formed by ejecta with different compositions.

8. Conclusions

We have presented multiband photometry of the massive GC NGC 6402 based on multiband HST observations collected as part of GO-16283 (PI: F. D'Antona). Our photometric diagrams have been combined with results from high-resolution spectroscopy (Johnson et al. 2019) to constrain the formation scenarios of multiple populations in GCs.

The huge gap in the distribution of some light elements (O, Mg, Al, and Na) found by Johnson et al. (2019) is certainly one of the most intriguing properties of multiple populations in NGC 6402. One of the main objectives of our work consists in exploring whether NGC 6402 lacks stellar populations with intermediate chemical composition, based on a large stellar sample. To do this, we exploit the ChM, which is a photometric diagram that has been previously used to identify and characterize multiple populations in 57 Galactic GCs as part of the HST UV legacy survey of GCs (Piotto et al. 2015; Milone et al. 2015, 2017). The main results of the new observations concerning the ChM are the following:

1. The ChM does not show stars with extreme chemical compositions as observed in some massive GCs (e.g., NGC 2808 and ω Cen). Notably, NGC 6402 lacks the E group stars of the prototype cluster NGC 2808.
2. The ChM contains a group of 2G stars (dubbed $2G_D$) on the red side of the diagram, indicating the presence of a small group of stars (~8%) having higher metallicity: NGC 6402 is then a Type II cluster, in the definition by Milone et al. (2017).
3. The ChM does not show any gaps. There is a region less populated in the middle region, between the extreme groups ($2G_C$ and $2G_A$). When we locate on the ChM a few giants in common with the spectroscopic sample, we find that there is an extreme star also among the less extreme group $2G_B$.

Thus it is very important to broaden the spectroscopic investigation of this cluster and study targets in the middle of the ChM.

An independent result of the observation is obtained in the parallel-field data: the CMD shows indeed a split MS, confirming that we are in the presence of a dichotomy in the helium abundance of the cluster stars. Therefore, the spectroscopic gap is fully confirmed by the presence of the MS gap. These results indicate that the cluster has undergone two stages of 2G star formation, the first one from matter strongly contaminated with p-processed elements and significantly rich in helium, and the second one from matter—not necessarily sharing the same heavy p-processing of the first event—heavily diluted with pristine gas, so that both the helium content and the abundances of light elements remain either standard or close to standard.

Already a simple superposition of the parallel-field data of NGC 2808 and NGC 6402 shows that the blue MS of the latter cluster is much less extreme, and thus its helium content is much lower than the $Y \sim 0.35$ attributed to the prototype cluster. In fact, the analysis of the MS data provides $Y \sim 0.31$ for this blue MS (and notice that the ChM analysis provides a similarly "low" $Y = 0.30$ for the extreme stars). This helium content for the extreme population is also consistent with the analysis of the HB.

The different samples examined give fractions of stars in the three main groups defined by spectroscopy (1G, mild 2G, and extreme 2G) reasonably compatible with each other, apart from the HB, which has far too few "red" stars, which should correspond to the 1G plus mild 2G sample. We will address this problem in a future study.

We find that the determination of a helium content $Y \sim 0.31$ for the 2G extreme stars is extremely useful, because it confirms the composition gap, and allows a more demanding comparison between models and abundances. We examine both the SMS model and the AGB model, and conclude that the present O–Na abundance patterns of the AGB yield for the metallicity of this cluster ($Z = 1.5 \times 10^{-3}$) are not compatible with $Y \sim 0.31$. Also present SMS models seem to be not compatible with the data, but we leave some space to further exploration of the parameter space: (i) the SMS mass—or the core temperature of nuclear processing—and (ii) the helium content at which the evolution of the SMS is artificially stopped.

Concerning the AGB model, we conclude that models allowing for a larger oxygen depletion preserving sodium are needed to be compatible with the data. Whether and under which hypotheses this is possible is to be explored. Anyway, it is difficult to maintain the hypothesis that the most extreme oxygen abundances found in GCs are simply due to deep mixing in the high-helium red giants, favored by the small chemical discontinuity left by convection at the first dredge-up (D'Antona & Ventura 2007).

One bonus of having established the degree of oxygen depletion necessary for the 1G ejecta polluting the extreme star sample is the following: the polluters of the 2G population will probably cover a range of oxygen depletion, from the most extreme value [O/Fe] ~ -1, to the moderate depletion shown by the AGB models. Consequently, after dilution with pristine gas, the gas forming the 2G mild stars may also cover a range of nitrogen abundances able to smooth down any gap in the ChM.

This work has received funding from the European Research Council (ERC) under the European Union's Horizon 2020 research innovation program (grant agreement ERC-StG 2016, No. 716082, "GALFOR"; PI: A.P.M.; http://progetti.dfa.unipd.it/GALFOR). A.P.M. acknowledges support from MIUR through the FARE project R164RM93XW SEMPLICE (PI: A.P.M.).

A.P.M. has been supported by MIUR under PRIN program 2017Z2HSMF (PI: Bedin). M.T. acknowledges support from the ERC Consolidator Grant funding scheme (project ASTEROCHRONOMETRY, G.A. No. 72293, http://www.asterochronometry.eu). Support for Program No. HST-GO-16283 was provided through a grant from the STScI under NASA contract NAS5-26555. EV acknowledges support from NSF grant AST-2009193. We thank the referee for suggestions and for a very careful reading of the manuscript.

ORCID iDs

Francesca D'Antona https://orcid.org/0000-0003-4697-0945
Antonino P. Milone https://orcid.org/0000-0001-7506-930X
Paolo Ventura https://orcid.org/0000-0002-5026-6400
Anna Fabiola Marino https://orcid.org/0000-0002-1276-5487

References

Amaro-Seoane, P., Konstantinidis, S., Brem, P., & Catelan, M. 2013, MNRAS, 435, 809
Anderson, J., & Bedin, L. R. 2010, PASP, 122, 1035
Anderson, J., Sarajedini, A., Bedin, L. R., et al. 2008, AJ, 135, 2055
Bastian, N., & Lardo, C. 2018, ARA&A, 56, 83
Bedin, L. R., Piotto, G., Anderson, J., et al. 2004, ApJL, 605, L125
Bekki, K. 2011, MNRAS, 412, 2241
Bekki, K., & Tsujimoto, T. 2016, ApJ, 831, 70
Bekki, K., & Tsujimoto, T. 2017, ApJ, 844, 34
Bellini, A., Anderson, J., & Bedin, L. R. 2011, PASP, 123, 622
Bellini, A., & Bedin, L. R. 2009, PASP, 121, 1419
Bellini, A., Milone, A. P., Anderson, J., et al. 2017, ApJ, 844, 164
Bellini, A., Piotto, G., Bedin, L. R., et al. 2009, A&A, 507, 1393
Brown, T. M., Cassisi, S., D'Antona, F., et al. 2016, ApJ, 822, 44
Brown, T. M., Taylor, J. M., Cassisi, S., et al. 2017, ApJ, 851, 118
Calura, F., D'Ercole, A., Vesperini, E., Vanzella, E., & Sollima, A. 2019, MNRAS, 489, 3269
Carretta, E. 2015, ApJ, 810, 148
Carretta, E. 2021, A&A, 649, A154
Carretta, E., Bragaglia, A., Gratton, R. G., et al. 2009, A&A, 505, 117
Carretta, E., Bragaglia, A., Lucatello, S., et al. 2018, A&A, 615, A17
Cohen, J. G., & Kirby, E. N. 2012, ApJ, 760, 86
Contreras Peña, C., Catelan, M., Grundahl, F., Stephens, A. W., & Smith, H. A. 2013, AJ, 146, 57
Contreras Peña, C., Catelan, M., Grundahl, F., Stephens, A. W., & Smith, H. A. 2018, AJ, 155, 116
Da Costa, G. S., Norris, J. E., & Yong, D. 2013, ApJ, 769, 8
Dalessandro, E., Cadelano, M., Vesperini, E., et al. 2019, ApJL, 884, L24
D'Antona, F., Bellazzini, M., Caloi, V., et al. 2005, ApJ, 631, 868
D'Antona, F., & Caloi, V. 2004, ApJ, 611, 871
D'Antona, F., & Caloi, V. 2008, MNRAS, 390, 693
D'Antona, F., Caloi, V., Montalbán, J., Ventura, P., & Gratton, R. 2002, A&A, 395, 69
D'Antona, F., & Ventura, P. 2007, MNRAS, 379, 1431
D'Antona, F., Vesperini, E., D'Ercole, A., et al. 2016, MNRAS, 458, 2122
Dell'Agli, F., García-Hernández, D. A., Ventura, P., et al. 2018, MNRAS, 475, 3098
Denissenkov, P. A., & Hartwick, F. D. A. 2014, MNRAS, 437, L21
Denissenkov, P. A., VandenBerg, D. A., Hartwick, F. D. A., et al. 2015, MNRAS, 448, 3314
D'Ercole, A., D'Antona, F., Carini, R., Vesperini, E., & Ventura, P. 2012, MNRAS, 423, 1521
D'Ercole, A., D'Antona, F., & Vesperini, E. 2016, MNRAS, 461, 4088
D'Ercole, A., Vesperini, E., D'Antona, F., McMillan, S. L. W., & Recchi, S. 2008, MNRAS, 391, 825
Dondoglio, E., Milone, A. P., Lagioia, E. P., et al. 2021, ApJ, 906, 76
Ferraro, F. R., Massari, D., Dalessandro, E., et al. 2016, ApJ, 828, 75
Ferraro, F. R., Pallanca, C., Lanzoni, B., et al. 2021, NatAs, 5, 311
Forbes, D. A., Bastian, N., Gieles, M., et al. 2018, RSPSA, 474, 20170616
Frischknecht, U., Hirschi, R., Pignatari, M., et al. 2016, MNRAS, 456, 1803
Frischknecht, U., Hirschi, R., & Thielemann, F. K. 2012, A&A, 538, L2
Gavagnin, E., Mapelli, M., & Lake, G. 2016, MNRAS, 461, 1276
Gieles, M., Charbonnel, C., Krause, M. G. H., et al. 2018, MNRAS, 478, 2461
Gratton, R., Bragaglia, A., Carretta, E., et al. 2019, A&Ar, 27, 8
Grundahl, F., Catelan, M., Landsman, W. B., Stetson, P. B., & Andersen, M. I. 1999, ApJ, 524, 242
Harris, W. E. 1996, AJ, 112, 1487
Johnson, C. I., Caldwell, N., Michael Rich, R., Mateo, M., & Bailey, J. I. 2019, MNRAS, 485, 4311
Johnson, C. I., Rich, R. M., Pilachowski, C. A., et al. 2015, AJ, 150, 63
Khoperskov, S., Mastrobuono-Battisti, A., Di Matteo, P., & Haywood, M. 2018, A&A, 620, A154
Lacchin, E., Calura, F., & Vesperini, E. 2021, MNRAS, 506, 5951
Lagioia, E. P., Milone, A. P., Marino, A. F., & Dotter, A. 2019, ApJ, 871, 140
Lagioia, E. P., Milone, A. P., Marino, A. F., et al. 2021, ApJ, 910, 6
Lardo, C., Bellazzini, M., Pancino, E., et al. 2011, A&A, 525, A114
Lee, J.-W. 2015, ApJS, 219, 7
Lee, Y.-W., Demarque, P., & Zinn, R. 1994, ApJ, 423, 248
Lee, Y.-W., Joo, S.-J., Han, S.-I., et al. 2005, ApJL, 621, L57
Lim, D., Han, S.-I., Lee, Y.-W., et al. 2015, ApJS, 216, 19
Mackey, A. D., & van den Bergh, S. 2005, MNRAS, 360, 631
Marino, A. F., Villanova, S., Milone, A. P., et al. 2011, ApJL, 730, L16
Marino, A. F., Villanova, S., Piotto, G., et al. 2008, A&A, 490, 625
Marino, A. F., Milone, A. P., Przybilla, N., et al. 2014, MNRAS, 437, 1609
Marino, A. F., Milone, A. P., Renzini, A., et al. 2019, MNRAS, 487, 3815
Marino, A. F., Milone, A. P., Yong, D., et al. 2017, ApJ, 843, 66
Milone, A. P., Bedin, L. R., Piotto, G., & Anderson, J. 2009, A&A, 497, 755
Milone, A. P., Marino, A. F., Piotto, G., et al. 2012a, ApJ, 745, 27
Milone, A. P., Marino, A. F., Piotto, G., et al. 2015, ApJ, 808, 51
Milone, A. P., Marino, A. F., Renzini, A., et al. 2018, MNRAS, 481, 5098
Milone, A. P., Piotto, G., Bedin, L. R., et al. 2012b, A&A, 537, A77
Milone, A. P., Piotto, G., Bedin, L. R., et al. 2012c, ApJ, 744, 58
Milone, A. P., Piotto, G., Renzini, A., et al. 2017, MNRAS, 464, 3636
Momany, Y., Bedin, L. R., Cassisi, S., et al. 2004, A&A, 420, 605
Mucciarelli, A., Bellazzini, M., Merle, T., et al. 2015, ApJ, 801, 68
Muñoz, C., Villanova, S., Geisler, D., et al. 2020, MNRAS, 492, 3742
Nardiello, D., Libralato, M., Piotto, G., et al. 2018, MNRAS, 481, 3382
Piotto, G., Bedin, L. R., Anderson, J., et al. 2007, ApJL, 661, L53
Piotto, G., King, I. R., Djorgovski, S. G., et al. 2002, A&A, 391, 945
Piotto, G., Milone, A. P., Bedin, L. R., et al. 2015, AJ, 149, 91
Portegies Zwart, S. F., Baumgardt, H., Hut, P., Makino, J., & McMillan, S. L. W. 2004, Natur, 428, 724
Portegies Zwart, S. F., Makino, J., McMillan, S. L. W., & Hut, P. 1999, A&A, 348, 117
Prantzos, N., Charbonnel, C., & Iliadis, C. 2017, A&A, 608, A28
Renzini, A., D'Antona, F., Cassisi, S., et al. 2015, MNRAS, 454, 4197
Sabbi, E., Lennon, D. J., Anderson, J., et al. 2016, ApJS, 222, 11
Searle, L. 1977, in Evolution of Galaxies and Stellar Populations, ed. B. M. Tinsley, R. B. Larson, & G. D. Campbell (New Haven, CT: Yale University Observatory), 219
Searle, L., & Zinn, R. 1978, ApJ, 225, 357
Simioni, M., Milone, A. P., Bedin, L. R., et al. 2016, MNRAS, 463, 449
Sollima, A., Ferraro, F. R., Bellazzini, M., et al. 2007, ApJ, 654, 915
Sugimoto, D., & Makino, J. 1989, PASJ, 41, 1117
Tailo, M., D'Antona, F., Vesperini, E., et al. 2015, Natur, 523, 318
Tailo, M., Di Criscienzo, M., D'Antona, F., Caloi, V., & Ventura, P. 2016, MNRAS, 457, 4525
Tailo, M., Milone, A. P., Lagioia, E. P., et al. 2020, MNRAS, 498, 5745
Tailo, M., Milone, A. P., Lagioia, E. P., et al. 2021, MNRAS, 503, 694
Tailo, M., Milone, A. P., Marino, A. F., et al. 2019, ApJ, 873, 123
van den Bergh, S. 1996, ApJL, 471, L31
Ventura, P. 2010, in IAU Symp. 268, Light Elements in the Universe, ed. C. Charbonnel (Cambridge: Cambridge Univ. Press), 147
Ventura, P., & D'Antona, F. 2009, A&A, 499, 835
Ventura, P., D'Antona, F., Imbriani, G., et al. 2018, MNRAS, 477, 438
Ventura, P., D'Antona, F., Mazzitelli, I., & Gratton, R. 2001, ApJL, 550, L65
Ventura, P., Di Criscienzo, M., Carini, R., & D'Antona, F. 2013, MNRAS, 431, 3642
Wirth, H., Jerabkova, T., Yan, Z., et al. 2021, MNRAS, 506, 4131
Yong, D., Norris, J. E., Da Costa, G. S., et al. 2017, ApJ, 837, 176
Zennaro, M., Milone, A. P., Marino, A. F., et al. 2019, MNRAS, 487, 3239